

# Three-dimensional measurements of plasma parameters in an inductively coupled plasma processing chamber

Cite as: Phys. Plasmas 26, 103503 (2019); <https://doi.org/10.1063/1.5115415>

Submitted: 18 June 2019 . Accepted: 06 September 2019 . Published Online: 03 October 2019

Jia Han, Patrick Pribyl, Walter Gekelman , Alex Paterson, Steven J. Lanham , Chenhui Qu, and Mark J. Kushner 



View Online



Export Citation



CrossMark



**NEW**

**AVS Quantum Science**

A high impact interdisciplinary journal for **ALL** quantum science

**ACCEPTING SUBMISSIONS**



# Three-dimensional measurements of plasma parameters in an inductively coupled plasma processing chamber

Cite as: Phys. Plasmas **26**, 103503 (2019); doi: 10.1063/1.5115415

Submitted: 18 June 2019 · Accepted: 6 September 2019 ·

Published Online: 3 October 2019



View Online



Export Citation



CrossMark

Jia Han,<sup>1</sup> Patrick Pribyl,<sup>1</sup> Walter Gekelman,<sup>1</sup>  Alex Paterson,<sup>2</sup> Steven J. Lanham,<sup>3</sup>  Chenhui Qu,<sup>4</sup> and Mark J. Kushner<sup>4</sup> 

## AFFILIATIONS

<sup>1</sup>Department of Physics, University of California, Los Angeles, California 90095, USA

<sup>2</sup>LAM Research Corp., Fremont, California 94538, USA

<sup>3</sup>Chemical Engineering Department, University of Michigan, Ann Arbor, Michigan 48109-2122, USA

<sup>4</sup>Electrical Engineering and Computer Science Department, University of Michigan, Ann Arbor, Michigan 48109-2122, USA

## ABSTRACT

Inductively coupled plasmas (ICPs) are extensively used for materials processing and microelectronics fabrication. However, their electromagnetic properties have not been fully characterized. In this regard, we have performed fully three dimensional (3D), time dependent measurements of the magnetic field, electron density, and electron temperature for an ICP sustained in argon in an industrial reactor designed for plasma etching in microelectronics fabrication. These measurements were compared to modeling results. The plasma was generated using pulsed power delivered at 2 MHz by a planar coil. The magnetic field was measured using a three axis magnetic probe at 15 366 locations throughout the plasma volume during the H-mode portion of the pulse at temporal intervals of 2 ns. A swept Langmuir probe was used to measure plasma parameters at the same locations. The plasma density measurement was calibrated with line-integrated densities obtained using a 96 GHz interferometer. During a single radio frequency (RF) cycle, the 3D current density [derived from  $B(\vec{r}, t)$ ] is initially maximum just below the coil and moves downward toward the center of the chamber. Isosurfaces of current are nearly symmetric toroids. The total electric field, space charge field, and inductive electric field were derived and used to calculate the dissipated power, plasma current, and Poynting flux. Computer modeling of the experiment reproduces the phase dependent behavior. Animations showing the time dependent 3D measurements are presented in the supplementary material.

© 2019 Author(s). All article content, except where otherwise noted, is licensed under a Creative Commons Attribution (CC BY) license (<http://creativecommons.org/licenses/by/4.0/>). <https://doi.org/10.1063/1.5115415>

## I. INTRODUCTION

Radio frequency (RF) power is the primary source for generating plasmas for semiconductor materials processing. The two dominant configurations for delivering this power are capacitively coupled plasmas (CCPs) and inductively coupled plasmas (ICPs).<sup>1</sup> In the ICP configuration, power is electromagnetically delivered by antennas taking the form of external coils. In the stovetop geometry, the coils are flat spirals mounted on an insulating ceramic window which is usually the top of the vacuum system. The coils are driven at frequencies ranging from hundreds of kilohertz to tens of megahertz depending upon the application, pressure, and power. The incident electromagnetic wave from the antenna typically has a dominant component in the azimuthal direction and propagates in the axial direction. The wavelength is usually much longer than either the skin depth or the chamber, and

so propagation is in near field. Electrons in plasma, accelerated by the incident RF field, produce a harmonic current, which in turn generates a small magnetic field within the plasma. A key to understanding fundamental plasma transport in these systems is measuring quantities such as the plasma density, magnetic field, internal currents, and electric field throughout the plasma volume. These quantities determine the power deposition profile, which ultimately determines the uniformity of processing.

Investigations of electromagnetic properties of ICPs have been performed over the past two decades. The use of magnetic probes (B-dot), for example, is a well-established method to measure magnetic fields inside ICPs. Piejak *et al.*<sup>2</sup> used a B-dot probe to measure a single component of the B field in an annular plasma sustained in Ar at pressures of 3–300 mTorr powered by an internal solenoidal coil.

They assumed a one-dimensional plasma structure and that an axisymmetric plasma current flows only in the azimuthal direction. With these assumptions, other components of the magnetic field can be derived using Maxwell's equations. In a later work, Piejak<sup>3</sup> reports on measurements in a chamber having a stovetop coil similar to an industrial plasma etching reactor. The authors measured the distribution of electromagnetic fields along a vertical line at a fixed radius and showed that B-dot probe measurements in such a system can be erroneous if the physical probe dimensions are too large (e.g.,  $d_{\text{probe}}/d_{\text{chamber}} = 0.06$ ).

Hopwood *et al.*<sup>4</sup> also investigated one component of the magnetic field in a 13.56 MHz ICP sustained in 5 mTorr Ar using a stovetop coil contained in a "McKenzie bucket"<sup>5</sup> (i.e., the walls were lined with magnets to generate a confining cusp field). Radial scans at three different heights were used to show consistency with the skin depth (1.6–3.6 cm) of ion densities measured using a Langmuir probe. A simple model using Maxwell's equation was used to deduce the electric field from the measured magnetic field.

Using single component magnetic field measurements, El-Fayoumi and Jones<sup>6</sup> made the most thorough measurement inside the volume of the chamber—on a plane consisting of 608 locations. The radial magnetic field was deduced from the axial field measurement using  $\nabla \cdot \vec{B} = 0$  while assuming the azimuthal magnetic field to be zero. The experimental data were then fitted to polynomial functions.  $\nabla \times \vec{B} = \mu_0 \vec{J}$  was then used to determine a plasma current. The current formed a toroidal ring under the stovetop coil and axially translated several cm away from the coil during a quarter RF cycle.

Using symmetry arguments, Tuszewski<sup>7</sup> found that when operating in oxygen, the magnetic field extended further into the plasma than in Ar, reflecting the lower conductivity and longer skin depth in the attaching molecular gas. Srinivasan *et al.*<sup>8</sup> studied the effect of current nodes in the antenna. Ding *et al.*<sup>9</sup> found regions of negative and positive power absorption consistent with nonlocal electron transport and anomalous skin depths.

Two components of the magnetic field ( $B_r$  and  $B_z$ ) were measured along one radial and one vertical line by Godyak *et al.*<sup>10</sup> in an ICP sustained Ar plasma at pressures of 1–10 mTorr with a stovetop coil driven at 6.78 MHz. The work assumed azimuthal symmetry based on having equally spaced concentric antennas. Using the measured two components of the magnetic field, the current density was calculated by taking derivatives along the line, assuming  $\partial/\partial r$  was uniform as a function of height.<sup>10</sup> The current density peaked within 1 cm of the dielectric window adjacent to the antenna and reversed direction in a second layer 6–8 cm from the dielectric. The magnitude and relative phase of the magnetic field, measured by a vector voltmeter, also revealed second harmonic current flowing normally to the main azimuthal current due to the nonlinear effect associated with the rf magnetic field at fundamental frequency.<sup>11</sup>

Ostrikov *et al.*<sup>12</sup> investigated ICPs having a stovetop coil driven at 500 kHz operating in both E- and H-modes. (E-mode refers to conditions where power deposition by electrostatic capacitive coupling from the coil dominates. H-mode refers to conditions where power deposition is dominantly by absorbing the electromagnetic wave produced by the antenna.) They found that the axial magnetic field peaked in the center of the reactor, with the radial magnetic field being maximum under the coil at half radius. They also found a second harmonic contribution of the azimuthal component of magnetic field,

which was attributed to nonlinear interactions between the radial and axial magnetic field components.

These previous measurements of properties of low pressure ICPs have provided keen insights into their operation and established many of the fundamental operating principles of low pressure ICPs. However, in most cases, only a subset of plasma properties have been reported and rarely in multiple dimensions due to limitations in diagnostics. Advances in diagnostics now enable simultaneous measurements of nearly all plasma and electromagnetic properties of such ICPs in 3-dimensions (3D). In this work, the radio frequency (RF) magnetic field, plasma density, and electron temperature were measured in 3D throughout the volume of an ICP sustained in Ar powered by a stovetop coil. The theme of the results presented here is to provide a self-consistent set of 3D measurements for electron temperature, ion density, magnetic field and electric field components, Poynting vector flux, and power deposition, with the goal of providing new or refined insights into operation of ICPs. For example, these 3D measurements show that the plasma density, current density, and Poynting flux have maxima in different locations. Reversals in current density (and regions of negative power deposition) are observed during a single RF cycle and corroborated with modeling results.

The temporal and spatial dependence of the plasma parameters are discussed during one RF cycle after the plasma has reached a steady state during pulsed operation.<sup>13</sup> The experiment was performed in an industrial plasma chamber of the type used for plasma etching which was modified to enable probe access by adding a cylindrical extension below the ceramic window. The antenna and ceramic top were located at the same height as in the commercial device. However, the antenna diameter was reduced by 7 cm in order to investigate physics directly underneath it. The data presented here show the structure of the plasma current and total electric field during an RF cycle. These values were then used to calculate the power deposition in the plasma. The plasma conductivity was calculated from the current density measurements. Computer modeling of the device was performed to help in interpretation of the experimental data. Behavior during the turn-on and decay phases of pulsed operation will be presented in a forthcoming paper.

This manuscript is structured as follows: the experimental setup and diagnostics are described in Sec. II, which also contains a brief description of the model. Measurements of key parameters and quantities derived from them, and computational results, are presented in Sec. III. The measurements include plasma density and temperature (Langmuir probe and microwave interferometer), magnetic field (3-axis magnetic probe), and space charge electric field (emissive probe). The derived quantities are current density ( $\frac{1}{\mu_0} \nabla \times \vec{B}$ ), inductive electric field ( $-\frac{\partial \vec{A}}{\partial t}$  or Faraday's law), Poynting flux ( $\frac{1}{\mu_0} (\vec{E} \times \vec{B})$ ), and conductivity. Our concluding remarks are given in Sec. IV.

## II. DESCRIPTION OF THE EXPERIMENT AND MODEL

### A. Experiment

A schematic of the experimental apparatus is shown in Fig. 1(a), and an image of the experiment is shown in Fig. 1(b). The ICP consists of a cylindrical chamber (height = 17.2 cm and radius = 26 cm) producing argon plasmas at pressures of 10–50 mTorr. A three-turn circular stovetop antenna, mounted on top of a 2.8 cm thick alumina window, was connected to an RF generator operating at a 2 MHz

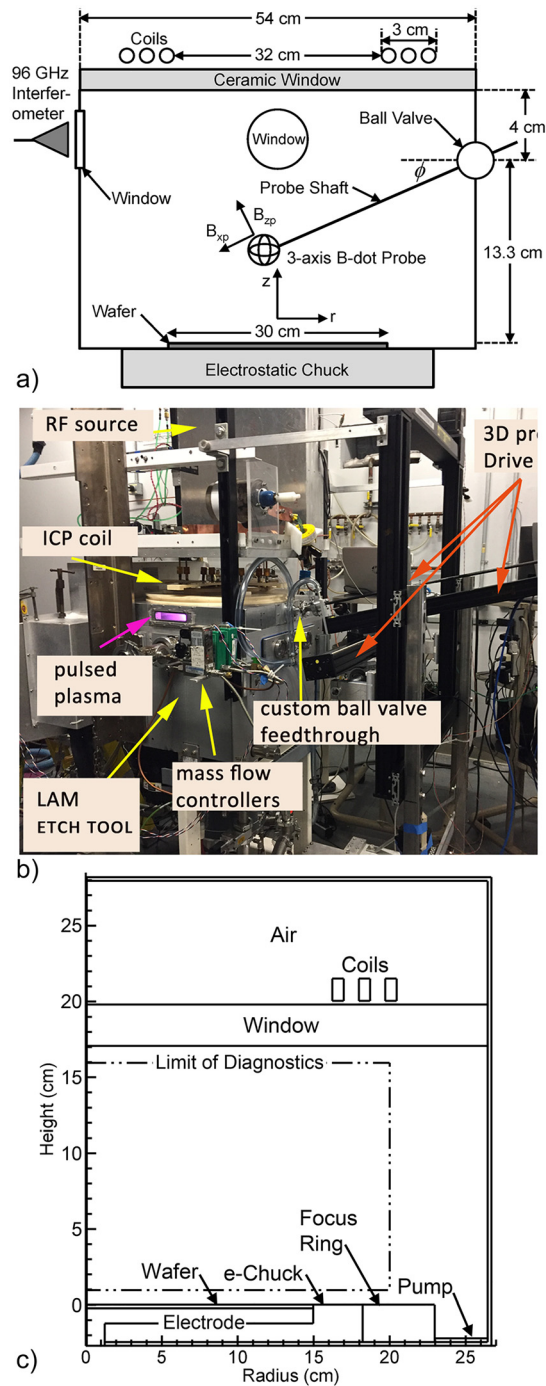


**FIG. 1.** Overview of the experimental setup and model geometry. (a) Schematic of the experimental chamber (not to scale). The probe shaft is capable of rotation and translation with the ball valve as the pivot point so that the probe tip can move in three dimensions inside the chamber. Here,  $B_{xp}$  is the x component of the magnetic field in the frame of the probe. (b) Photo of the experimental apparatus. When in use, the interferometer is positioned at the rectangular window through which the “pulsed plasma” is viewed. This window is 90° from the ball valve port. (c) Schematic of the cylindrically symmetric computational geometry.

delivering power up to 1 kW. The antenna is wired as two 1.5 turn coils connected in parallel. The coil has a center radius of 18 cm with three turns separated by 1.1 cm and is located at 21.6 cm above the wafer (one cm above the top surface of the dielectric). When producing a plasma with 300 W, the peak current in each conductor is approximately 18 A. A Si wafer 15 cm in radius was electrostatically clamped to the cylindrical chuck (radius = 22.75 cm) and cooled with backside helium flow. For measurements discussed in this paper, the top surface of the wafer is at axial location  $z = 0$ . The height of the plasma (wafer to the bottom of the ceramic window) is 17.2 cm. A mass flow controller sets the chamber gas pressure measured by convection and Pirani gauges. Unless otherwise noted, experimental data presented in this paper are acquired with a flow rate of 100 sccm. This matched the flow rate used in the simulations. In these experiments, there was no additional bias voltage applied to the substrate.

Probes were inserted from the front (load lock) side of the chamber through a ball valve feedthrough<sup>14</sup> allowing free rotation of the probe shaft through  $\theta$  and  $\phi$  spherical coordinates. The probe motion is driven by a 3D drive shown in Fig. 1(b). The stepping motors have embedded controllers and interface to a computer and can position the attachment point of the probe with a linear precision of 10  $\mu\text{m}$  along each drive. The probe tip can be located on a grid within the chamber precise to within 50  $\mu\text{m}$ , although there is up to a 0.5 cm difference between this grid position and chamber coordinates over the full extent of the 3D volume. The rotational limit on the ball valve and position of the port prevent the probe from reaching a region immediately adjacent to its mounting point. This is indicated by missing data in figures showing 2D planes of 3D data. Data were acquired using a 4 channel 2.5 GS/s, 12 bit oscilloscope. The probe motion and data acquisition systems were controlled by a Python program communicating with both through ethernet protocols. The plasma density, electron temperature, plasma potential, and all components of the magnetic field were typically measured on a two- or three-dimensional grid having 1 cm separation between points.

Plasma potential was measured using an emissive probe.<sup>15</sup> The probe consisted a thoriated tungsten filament heated by an isolated power supply with a low capacitance to ground.<sup>16</sup> Prior to making measurements, the probe temperature was adjusted so that the I-V curve of the probe was symmetric. The heater current to the probe was switched off for the duration of the measurement. The off period was typically a few milliseconds, which was measured to be too short a time for the probe emission to decay due to changes in temperature. The probe is capable of tracking changes in plasma potential below a frequency of about 20 MHz. This was verified using a signal generator and an external resistor. The value of the resistor matched  $dV/dI|_{I=0}$  obtained by sweeping the probe in its emissive state, which is assumed to be the connection resistance to the plasma when the probe is floating. During the steady state, the RF component of the plasma potential ranges from a few volts to a few tenths of a volt depending on the antenna power and probe position. Data collected by the probe were then used in calculating the space charge electric field,  $\vec{E} = -\nabla\phi_p$ .

A cylindrical Langmuir probe made from tungsten ( $l = 1.43$  mm,  $d = 0.28$  mm) was used to measure electron temperature and ion saturation current. Although bi-Maxwellian electron energy distributions have been observed in low pressure argon discharges,<sup>17</sup> we found that our measured distributions were well represented by a single-temperature Maxwellian. That is, a straight line was a good fit to the

log of the probe characteristic. Therefore, we assumed a simple Maxwellian electron energy distribution. The electron temperature ( $T_e$ ) is determined by fitting an exponential to the I-V curve with ion current subtracted.  $T_e$  varies  $\pm 0.2$  eV throughout the measurement volume, with an average of 3.0 eV during the steady state portion of the pulsed discharge. There was no overall trend to the spatial profile, indicating a uniform  $T_e$ . These results agree with previous measurements in similar devices using Thomson scattering.<sup>18</sup> As determined from the emissive probe measurement, RF oscillations in plasma potential are negligible in the bulk of the plasma, being confined by plasma shielding to the region within a few centimeters of the antenna.

The spatial profile of ion saturation current ( $I_{\text{isat}}$ ) was acquired using this Langmuir probe biased at  $-60$  V. The output signal was low-pass filtered at 160 kHz. Since the probe is biased at a voltage much larger than the RF fluctuation of the plasma potential, compensation is not necessary. With the measured uniform temperature, a relative density profile was calculated using  $I_{\text{isat}} = Ane\sqrt{\frac{kT_e}{M}}$ , where  $A$  is the area of the probe,  $M$  is the ion mass, and  $e$  is the elementary charge. We note that relative profiles so obtained were the same for probe bias between  $-20$  V and  $-60$  V, although the overall magnitudes were different. To eliminate the amplitude ambiguity, we cross-calibrated the measured profiles against the line integral electron density measured by a 96 GHz microwave interferometer. The results discussed in this paper all used this calibration. With a bias of  $-60$  V, the correction factor at 10 mTorr and RF power below 160 W was about 20%; at higher power, it dropped to 10%.

During a portion of this work, a hairpin probe<sup>19</sup> was also available for the local density measurement. The results are described in a separate publication<sup>20</sup> but closely track with the profiles inferred by the above technique.

A three-axis, single turn magnetic probe<sup>21</sup> ( $\approx 4$  mm diameter) was used to measure the RF magnetic field produced by the antenna on the same 1 cm spatial grid as the ion saturation current was acquired. The B-dot probe response was calibrated using a Helmholtz coil and a vector network analyzer. The RF magnetic field induces an electric field which, in turn, produces an RF current through the plasma. The data were analyzed by first integrating the three temporal signals recorded from the magnetic probe, as the probe response is proportional to  $\partial \vec{B} / \partial t$ . Due to the positioning of the ball-valve feed-through used for the vacuum penetration, the probe position is defined by two angles ( $\theta$ ,  $\phi$ ) as shown in Fig. 1(a) and the distance that the probe shaft extends into the chamber. The transformation to Cartesian coordinates inside the chamber is given by

$$\begin{bmatrix} B_x \\ B_y \\ B_z \end{bmatrix} = \begin{bmatrix} \cos \theta \cos \phi & -\sin \theta & \cos \theta \sin \phi \\ \sin \theta \cos \phi & \cos \theta & -\sin \theta \sin \phi \\ \sin \phi & 0 & \cos \phi \end{bmatrix} \begin{bmatrix} B_{xp} \\ B_{yp} \\ B_{zp} \end{bmatrix}, \quad (1)$$

$$\tan \theta = \frac{y}{(R_p + x)}, \quad \tan \phi = \frac{z}{(R_p + x)}$$

where  $R_p$  is the distance of the pivot point of the ball valve (slightly past the outer chamber edge) from the center of the chamber.  $\theta$  is the angle between the probe shaft in the  $x$ - $y$  plane and the  $x$  axis, and  $\phi$  is the angle from the plane  $z=0$ . This definition is convenient for the probe geometry and is notably not quite a spherical coordinate transformation.

The plasma was operated using pulsed power having a pulse repetition frequency of 100 Hz and a duty cycle of 50%, resulting in a power-on period of 5 ms. The current ramp-on and ramp-down times were 50  $\mu$ s. All quantities were measured after the plasma has reached a quasisteady state during the power pulse operating in H-mode. The temporal behavior of the optical emission from the plasma was captured with a Si photodiode sensitive to visible light and near infrared. The photodiode has a response time of 1  $\mu$ s and viewed the center of the plasma.

## B. Description of the model

Properties of the ICP were modeled using the Hybrid Plasma Equipment Model (HPEM).<sup>22</sup> The HPEM is a simulator that combines modules addressing different physical phenomena in a time slicing manner. The modules used in this investigation are the Electromagnetics Module (EMM), Electron Monte Carlo Simulation (eMCS), and the Fluid Kinetics Module (FKM). Harmonic electromagnetic fields launched from the coil are produced in the EMM by solving the frequency domain wave equation. Continuity, momentum, and energy equations for ions and neutral particles, continuity and momentum equations for electrons, and Poisson's equation for the electric potential are integrated in time in the FKM. RF electric and magnetic fields from the EMM and electrostatic fields from the FKM are then used in the eMCS to advance pseudoparticle trajectories produce electron energy distributions as a function of position including electron-electron collisions. These distributions are then used to produce electron transport coefficients and electron impact rate coefficients for use in other modules. The argon reaction mechanism used in the model is the same as described by Tian *et al.*<sup>23</sup> The geometry is 2-dimensional in cylindrical coordinates assuming azimuthal symmetry.

To account for collisionless electron heating and anomalous skin effects in absorption of the coil-launched electromagnetic wave in the plasma, electron currents are calculated in the eMCS and used in the EMM in solution of the wave equation.<sup>24</sup> The solution to the wave equation in the EMM is performed in the frequency domain, while advancement of pseudoparticle trajectories in the eMCS is performed in the time domain. Electron currents are computed in the eMCS by collecting statistics on the azimuthal component of velocity of the electron pseudoparticles as a function of position and time. These statistics are then Fourier analyzed to provide the harmonic electron current density as a function of position and time,

$$J_\phi(\vec{r}, t) = J_\phi(\vec{r}) \text{Re}(e^{i(\omega t + \delta_j(\vec{r}))}), \quad (2)$$

where  $J_\phi(\vec{r})$  is the local harmonic amplitude of the current density and  $\delta_j(\vec{r})$  is the phase of the current density. This current density is then used in the EMM to solve the frequency domain wave equation,

$$\nabla^2 E_\phi(\vec{r}) + \left(\frac{\omega}{c}\right)^2 E_\phi(\vec{r}) = i\omega\mu_0 J_\phi(\vec{r}), \quad (3)$$

to produce the time and spatially dependent electric field in the azimuthal direction,

$$E_\phi(\vec{r}, t) = E_\phi(\vec{r}) \text{Re}(e^{i(\omega t + \delta_E(\vec{r}))}), \quad (4)$$

where  $E_\phi(\vec{r})$  is the harmonic amplitude of the electric field and  $\delta_E(\vec{r})$  is the phase of the electric field. In cases where electron

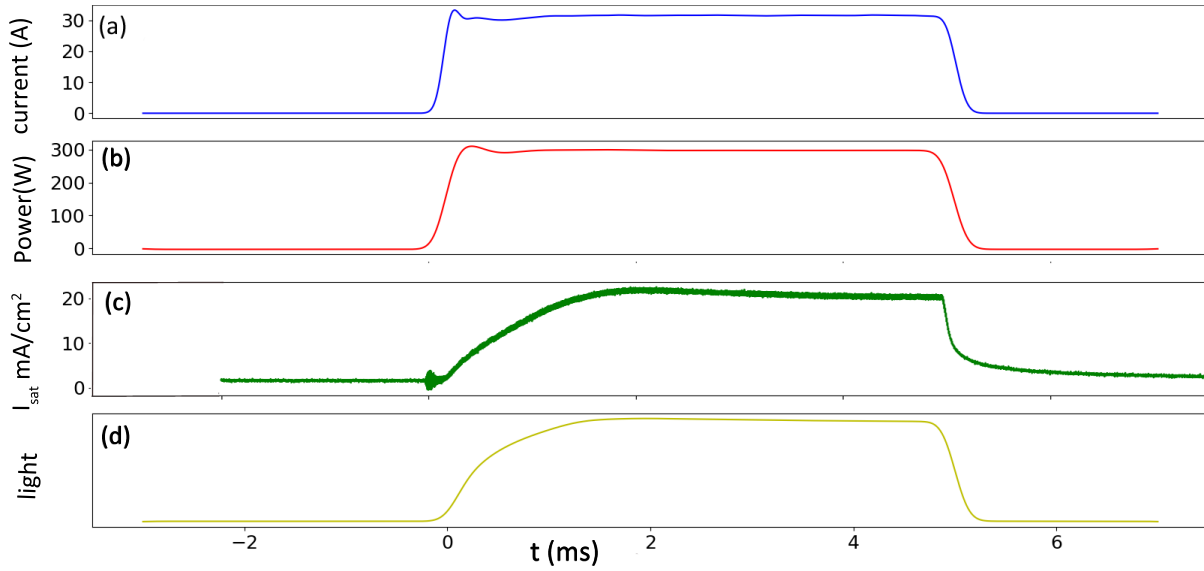


**FIG. 2.** Plasma properties during a pulsed cycle. (a) Current in the 3-turn RF antenna. (b) Power from the RF generator. (c) Ion saturation current measured by the Langmuir probe located at  $z = 12$  cm,  $r = 0$  cm. (d) Photodiode signal measuring optical emission positioned at a window facing the center of the plasma. The slower decay in  $I_{\text{sat}}$  compared to the optical signal indicates more rapid thermalization of the electron temperature than losses of ions by diffusion to the walls.

heating is approximated as being solely collisional, the current density is given by

$$J_{\phi}(\vec{r}, t) = \sigma(\vec{r})E_{\phi}(\vec{r}, t), \tag{5a}$$

$$\sigma(\vec{r}) = \frac{n_e(\vec{r})e^2}{m_e\nu_m(\vec{r})\left(1 + i\frac{\omega}{\nu_m(\vec{r})}\right)}, \tag{5b}$$

where  $n_e$  is the electron density,  $\sigma$  is the conductivity,  $m_e$  is the electron mass, and  $\nu_m$  is the momentum transfer collision frequency. The radial and axial components of the magnetic fields are then obtained from Faraday’s law. The instantaneous power deposition is

$$P(\vec{r}, t) = J_{\phi}(\vec{r}, t)E_{\phi}(\vec{r}, t). \tag{6}$$

The geometry used in the model is shown in Fig. 1(c). In the model, the ceramic window having a negligible conductivity also serves

as a showerhead for injection of argon gas at 100 sccm for a pressure of 10 mTorr. The three turn coil sits a few mm above the window. The Si wafer sits on a metal, grounded substrate surrounded by an alumina electrostatic chuck and a focus ring. Gas is annularly pumped outside the focus ring. The outer boundary of the chamber is grounded. The limit of the experimental diagnostics is shown by the dashed-dotted line.

Since the HPEM is a modular simulator that is intended to address a wide variety of plasma sources, computational parallelization is difficult. In all modules, there are computational branching points invoking different algorithms to address, for example, transport in magnetized or not-magnetized plasmas. This is particularly the case in the eMCS where the transport algorithms are divided into many loops each performing a relatively small amount of work. Parallelizing these smaller loops does not result in significant improvement in performance due to the computational overhead in repeatedly launching (and terminating) these small parallel loops.

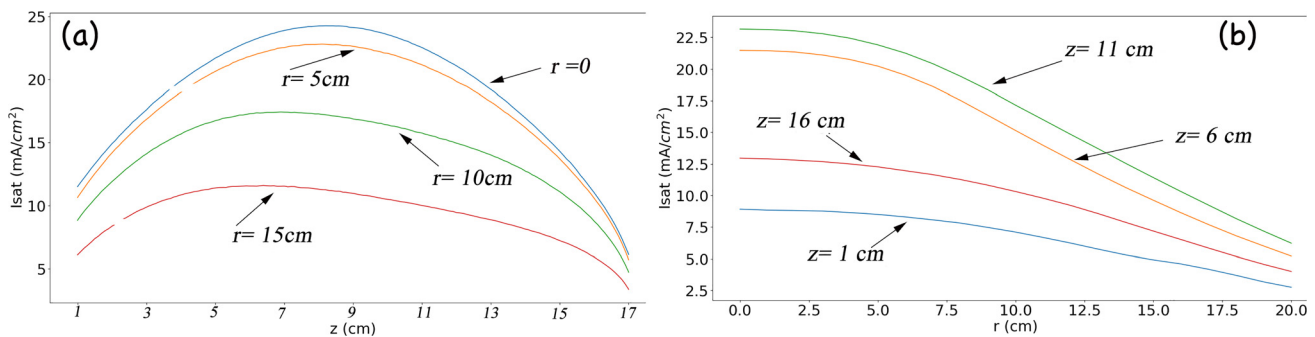


**FIG. 3.** Measurements of plasma density for Ar 10 mTorr and a generator power of 300 W. (a) Density as a function of height above the wafer at different radii. (b) Density as a function of radius at different heights.

Due to the modular nature of the HPEM, obtaining efficient computational parallel performance is challenging. A different parallelization strategy is required for each module (and submodules) which makes parallelization over large numbers of processors impractical. When implemented in parallel using 5–10 processors, as in the cases discussed here, speedups of factors of 3–5 over serial can be obtained. (Using additional processors typically does not improve performance.) To improve parallel performance in the eMCS module, the eMCS was restructured in the following manner.

The eMCS module consists of initialization subroutines (IS), particle trajectory and collisions subroutines (PS), and diagnostic and postprocessing subroutines (DPS). On each call to the eMCS, the IS are called, followed by several calls to the PS. Following each call to the PS, there is a call to the DPS. Residing within the PS are many smaller loops/branches, needed for generality, which slow parallel performance if they are individually made parallel. The restructuring consisted of executing the entire set of PS routines as a parallel thread without any internal parallelization. For example, outside the PS, an array of particle properties is  $A(i)$ , for the  $i$ th particle. Entering into IS, particles and their property arrays are allocated into thread aware arrays,  $A_T(i,j)$ , where  $i$  is the particle number and  $j$  is the thread. When executing the PS, parallel threads are launched which separately operate on  $A_T(i,j)$  without memory collisions. Upon completion of PS, the  $A(i)$  are reconstructed from the  $A_T(i,j)$ . Since there are still overhead costs with the allocation and reconstruction operations, the restructured eMCS is not efficient when using small numbers of particles. For those conditions, the prior parallelization of individual loops inside PS is more efficient. However, with large numbers of particles, the restructured eMCS is significantly more efficient.

### III. PLASMA PROPERTIES

The evolution of plasma properties during the power pulse is shown in Fig. 2. The fill pressure was 10 mTorr. The plasma transitions through the E-mode to H-mode during the first 0.5 ms of the pulse. Subsequently with constant power input in H-mode, the plasma density builds up and reaches a steady state in approximately 2 ms. The initial overshoot visible in the power waveform is due to the controller.

#### A. Plasma density

As described above, electron density profiles computed from ion saturation current assuming a uniform spatial electron temperature and calibrated by an interferometer are shown in Fig. 3. Plasma density peaks in the center of the reactor both radially and vertically, which is contrary to our expectation that plasma density would be off-set toward the top of the device and under the RF antenna where power deposition is maximum. Density contours on an  $(r,z)$  plane for

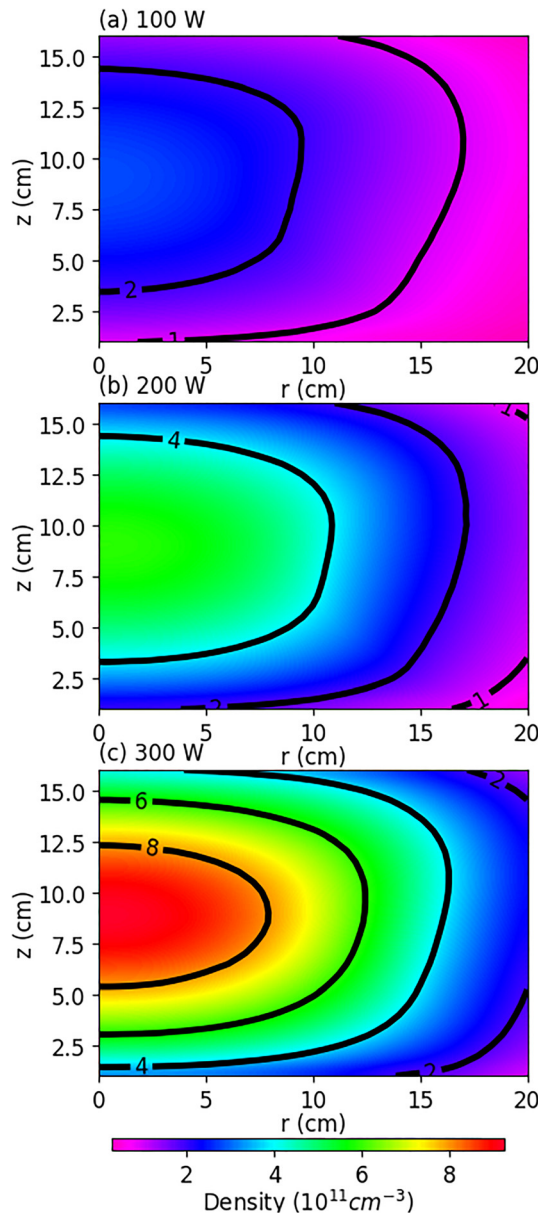


FIG. 4. Electron density in an  $(r,z)$  plane for three generator powers. The density is evaluated from the interferometer calibrated  $I_{sat}$  assuming uniform  $T_e = 3$  eV. The edge of the wafer is at  $r = 15$  cm.

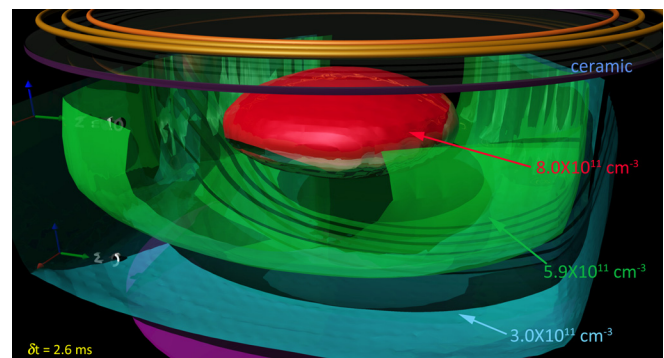


FIG. 5. 3D measurement of electron density derived from ion saturation current shown as nested isosurfaces. Data were acquired 2.6 ms into the 300 W power pulse. The wafer is drawn to scale to guide the eye. The maximum electron density at this time (red surface in center) is  $8 \times 10^{11} \text{ cm}^{-3}$ .

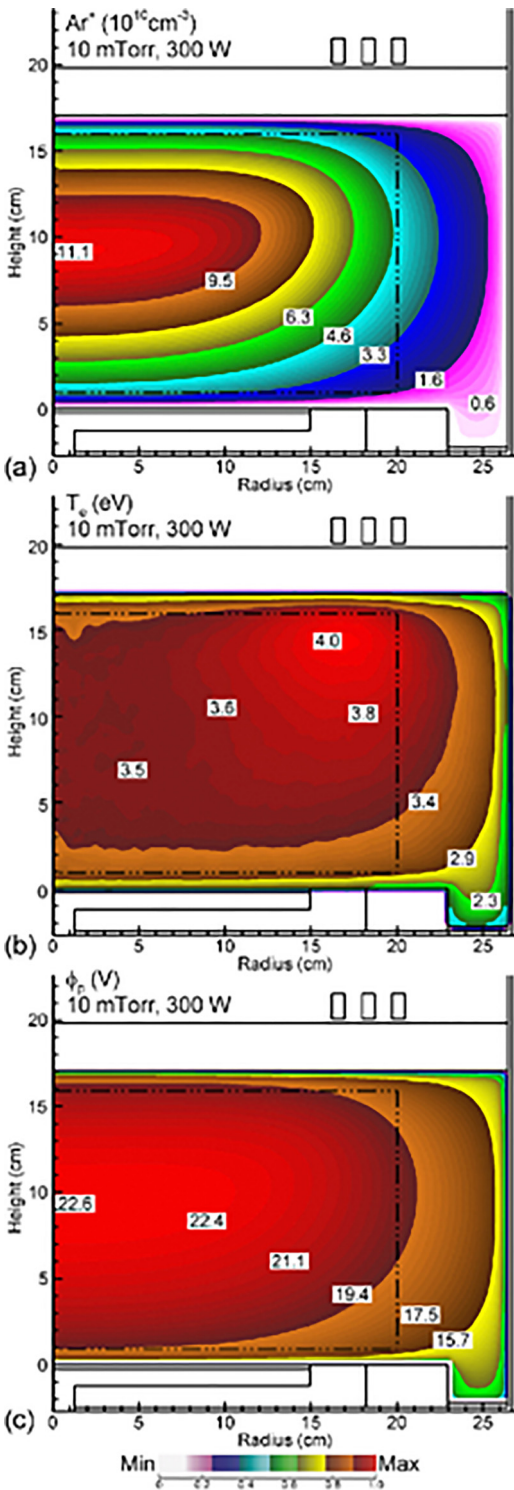


FIG. 6. Plasma properties predicted by the model for the ICP sustained in argon at 10 mTorr and 300 W. (a)  $\text{Ar}^+$  density (contours have units of  $10^{10} \text{ cm}^{-3}$ ), (b) electron temperature, and (c) plasma potential. The dashed-dotted line represents the experimental viewing area.

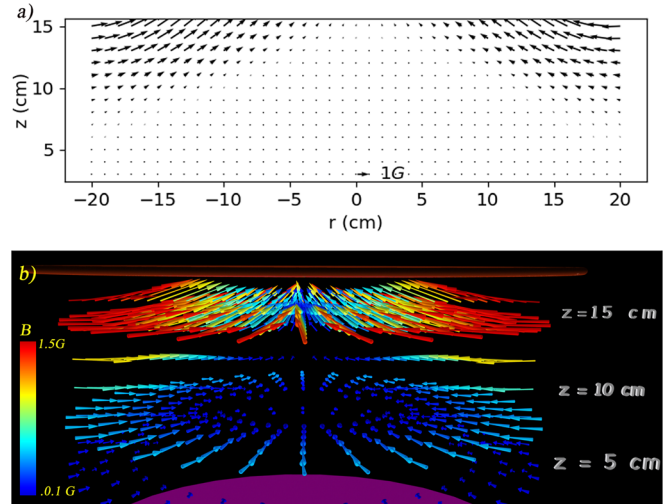


FIG. 7. Measured magnetic field during the steady state plasma. (a) 2D vector plot ( $r \leq 20 \text{ cm}$ ). The fiducial arrow represents a magnitude of 1 G. Note the coil is centered at 18 cm. (b) 3D vector plot ( $r \leq 15 \text{ cm}$ ). The coils and wafer are drawn to scale to aid the eye. The largest arrow drawn in red is  $|B| = 1.5 \text{ G}$ .

three generator powers are shown in Fig. 4. The maximum density at 300 W is  $9.0 \times 10^{11} \text{ cm}^{-3}$ . Density increases with power, but the position of peak density is nearly independent of power.

The electron density is shown in Fig. 5 in a 3D perspective; data were acquired at 15 366 spatial locations throughout the volume having separations on a cubic grid of 1 cm. Measurements were made for 64 000 time steps over 269 RF cycles. Several isosurfaces of constant  $I_{sat}$  are drawn in Fig. 5 at 2.3 ms after the start of the power pulse. Unlike other quantities such as the internal electric field, which varies at the 2 MHz frequency, the plasma density at any one location is essentially constant over the RF cycle. The plasma first forms under the coil at the start of the pulse and then moves inward to become the spatial distribution shown in Fig. 5. This motion takes about 1 ms.

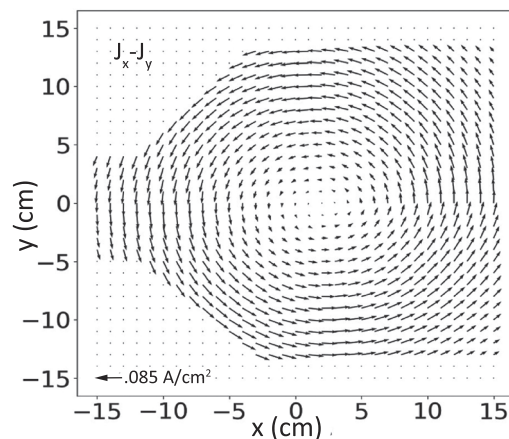


FIG. 8. Plasma current density in a plane-parallel to and 8 cm above the wafer in the steady state H-mode at the time of maximum current over a 2 MHz cycle.

As mentioned in Sec. I, the temporal evolution of this and other quantities will be presented in a subsequent work.

Computed plasma properties (cycle averaged  $\text{Ar}^+$  density, electron temperature, and plasma potential) for 300 W power deposition are shown in Fig. 6. As measured in the experiments, early during the pulse, the plasma density is maximum under the coil and transitions toward the axis. This transition results from two dominant effects. The first is an increase in plasma density which increases the electron thermal conductivity. The higher thermal conductivity enables power deposition that is maximum under the coil to heat electrons throughout the reactor. The second is an increase in the argon metastable density, which assumes a diffusion dominated profile that peaks near the center of the plasma. The lower threshold for multi-step ionization from the  $\text{Ar}^*$  diminishes the importance of the elevation of the tail of the electron energy distribution function (EEDF) that occurs in the skin depth of the ICP. The predicted electron temperature is relatively uniform, in the bulk plasma within the viewing volume of the experiment, 3.5–3.6 eV, and elevated to 4.0 eV within the skin depth (outside the experimental view area). This electron temperature is 0.5 eV higher than measured, but within experimental bounds.

### B. Magnetic field and plasma current density

A snapshot of the vector magnetic field at one instant of time is shown in Fig. 7. The Ar pressure is 10 mTorr, and the generator power is 300 W. The measurements are made at 2 ms after the start of the power pulse when the plasma is in steady state H mode (see Fig. 2).

The plasma current density is derived from the measured magnetic field using  $J = \frac{1}{\mu_0} \nabla \times \vec{B}$ . The gradient calculation is performed by either a three-point quadratic Lagrangian interpolation (IDL) or a 1st or 2nd order finite difference method. The three methods give nearly identical results. The currents as a 2D vector plot in an x-y plane-parallel to and 8 cm above the wafer are shown in Fig. 8. Currents flow in the azimuthal direction, reversing sign every half-cycle of the 500 ns RF period. Directly under the antenna, this component of the plasma current is  $180^\circ$  out of phase with the antenna current, as expected from Lenz’s law. The missing vectors on the left hand side of Fig. 8 reflect spatial positions that cannot be

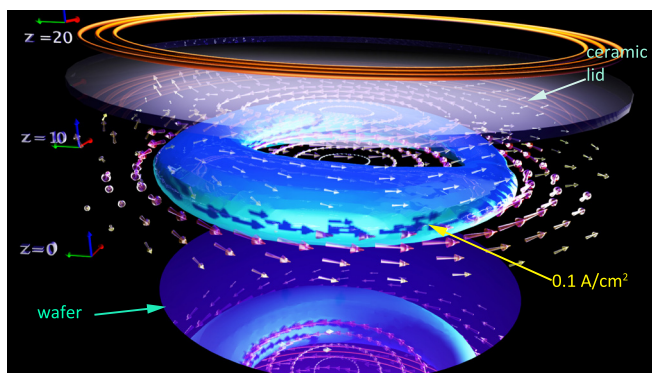


FIG. 9. Plasma current density during the quasisteady state of the power pulse at  $t = 3.3$  ms after the start of the pulse. The Ar pressure is 10 mTorr, and the generator power is 300 W. The current is derived from the measured magnetic field. The blue shell is an isosurface of constant current density ( $J = 0.1 \text{ A/cm}^2$ ). The RF current in the 3 coils, drawn to scale at the top, is close to the peak value of 35 A.

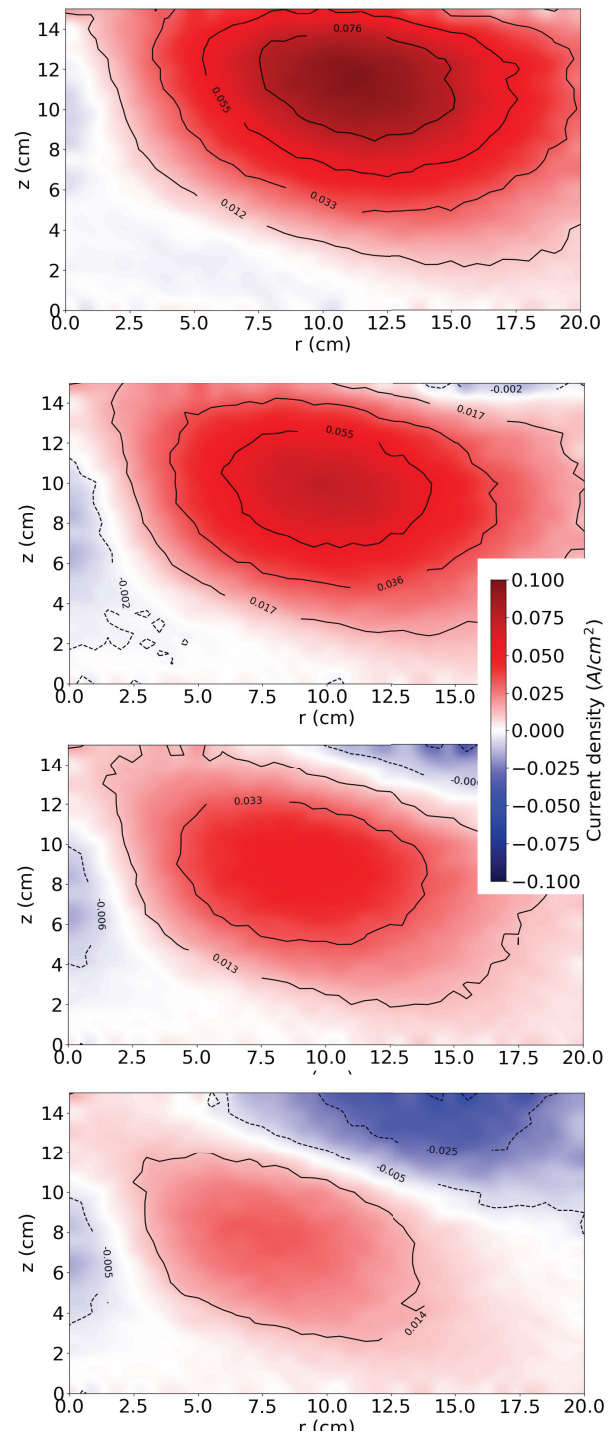


FIG. 10. Plasma current density ( $\text{A/cm}^2$ ) in a vertical ( $r, z$ ) plane at four times during the RF cycle. The Ar pressure is 10 mTorr, and the generator power is 300 W. The images from top to bottom are at times,  $t/T_{\text{rf}} = 0, 0.13, 0.19,$  and  $0.25$ , respectively. The internal current forms below the coil ( $z = 21.6 \text{ cm}$  and  $r = 16.0 \text{ cm}$ ) and moves down and toward the center of the chamber. The reverse current (shown in blue) forms as the current in the center fades away.

reached by the probe which penetrates the chamber from the left side. The azimuthal currents are approximately ten times larger than the radial or axial currents. Note that for the missing data points, the plasma current density is symmetric about the origin—the radial center of the chamber.

A 3D representation of the measured current is displayed in Fig. 9. To compensate for the missing data in Fig. 8 due to probe access, data from  $x = 0$  to 15 cm were used, assuming left-right symmetry. This symmetrized data are used to derive the Poynting flux and power dissipation discussed in Sec. III E. The peak antenna current is 37 A distributed over three turns. In contrast, the peak plasma current obtained from spatially integrating the current density in Fig. 9 is 12 A. This value is consistent with Fig. 7 where most of the magnetic field lines from the antenna do not intercept the bulk of the plasma.

The azimuthal plasma current density is shown in Fig. 10 sampled at 4 times during a quarter-cycle of an RF period in a vertical

plane. The generator power is 300 W. The images are for  $t/T_{rf} = 0, 0.13, 0.19,$  and  $0.25$ , where  $T_{rf}$  is the RF period, and were chosen to illustrate the dynamics of the current penetration into the plasma. The dynamics resemble eddy current penetration into a conductor from the external driving current. Since the internal electric field that drives the current changes sign every half cycle, the plasma current directly under the coil reverses and gains strength as the previous current maximum decays and moves downward. Note that for this figure, the flow rate was reduced to 25 sccm to better emphasize the current penetration, as further discussed in Sec. III D. This current diffusion pattern was seen by Fayoumi<sup>6</sup> and described as “the Ohmic response of the plasma due to an external driving current.”

Model predictions for current density as a function of phase for similar conditions are shown in Fig. 11. The initial phase in this sequence was chosen to align with that of the experiment. Following that alignment, the time between frames is the same as the experiment.

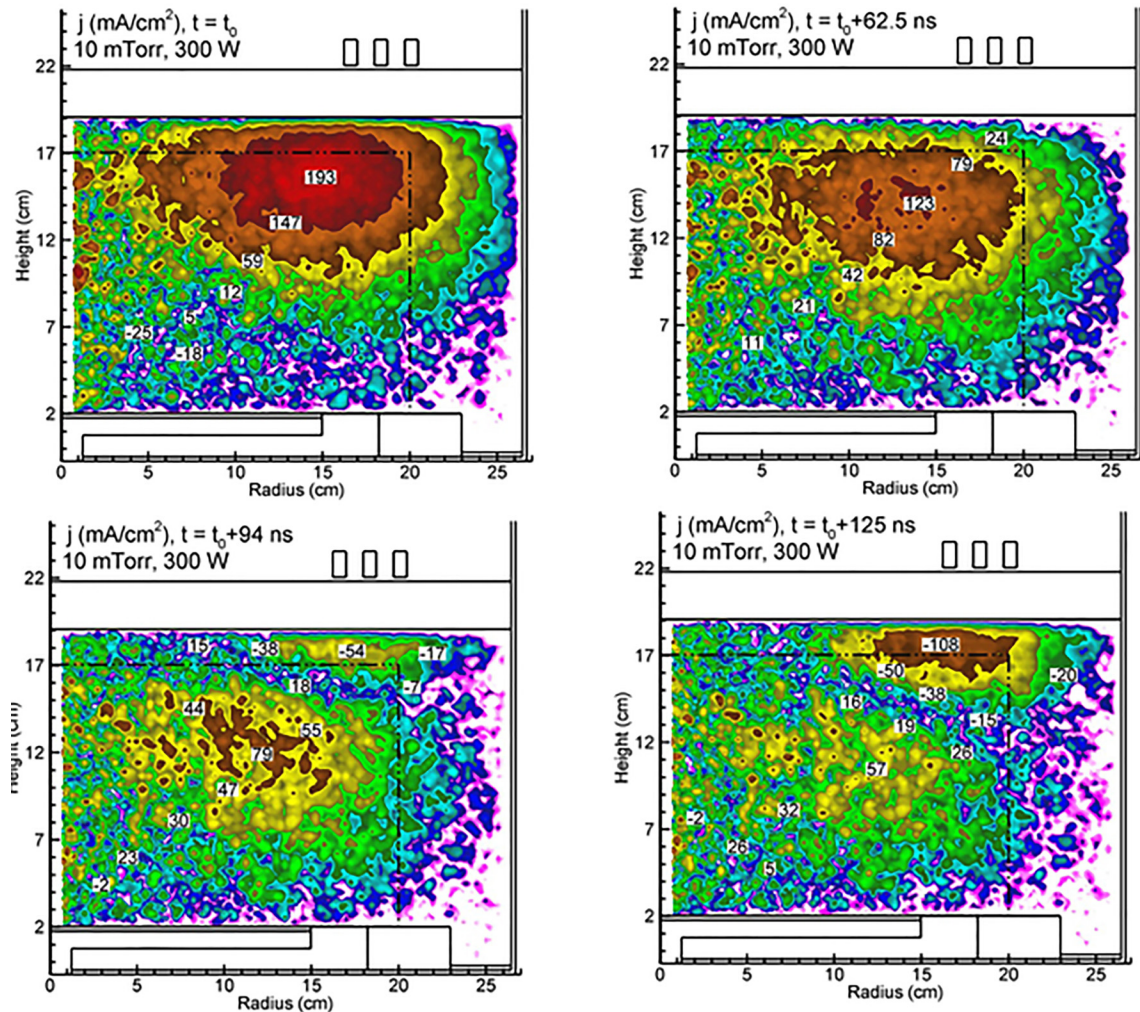


FIG. 11. Plasma current density in  $(\text{mA}/\text{cm}^2)$  plotted on a log scale at four times during the RF cycle, aligning with the experimental results in Fig. 11. The Ar pressure is 10 mTorr, and the power deposited in the plasma is 300 W. The images are (a)  $t_0$ , (b)  $t_0 + 62.5$  ns, (c)  $t_0 + 93.75$  ns, and (d)  $t_0 + 125$  ns. The dashed-dotted line is the experimental view.

The experimental trends of both current reversal and simultaneous regions of positive and negative current densities are also predicted by the model. The origins of the simultaneous regions of positive and negative current densities are twofold. First, the reactive or inertial component of the plasma conductivity, which is proportional to  $\omega/\nu_m$ , introduces a phase delay between the velocity of the electrons (which dominate the current density) and that of the incident electric field. In the limit that  $\omega \gg \nu_m$ , the plasma conductivity is dominated by reactance, and electron velocities are  $90^\circ$  out of phase with the incident electric field. In the limit that  $\omega \ll \nu_m$ , the plasma conductivity is dominated by resistance, and electron velocities are in phase with the incident field. The finite response time of the electrons to reversals in the electric field then leads to regions in which current density is opposite to the incident electric field. (To emphasize these reversals, the computed results in Fig. 11 are plotted on a log-scale, whereas the experimental results are plotted on a linear scale.) These out-of-phase electrons also result in negative power deposition, discussed below.

### C. Electric field

The manner of power transfer from the ICP coil to the plasma is important for understanding the plasma dynamics. For example, in addition to power being deposited in the plasma, power delivered from the generator is dissipated by the resistance of the coil, radiated into free space, and consumed by eddy losses in the metal of the chamber. To unambiguously determine the power dissipated in the plasma, one should measure the internal electric fields so that  $\vec{J} \cdot \vec{E}$  can be volume integrated. Here, we present measurements of the total internal electric field derived from measurement of the magnetic fields (electromagnetic component) and plasma potential (electrostatic component). The total electric field is given by  $\vec{E} = -\nabla\phi_p - \frac{\partial\vec{A}}{\partial t}$ , where  $\phi_p$  is the electrostatic plasma potential and  $\vec{A}$  is the vector potential. We first discuss the electrostatic component.

In the collisional, low temperature plasma represented by this system, charge neutrality is maintained by self-generated ambipolar electric fields, which constrain electron and ion fluxes to surfaces to be equal. The ambipolar electric fields, generally pointing from the center

to the boundaries of the plasma, are produced by a small positive space charge in the plasma (leading to the description electropositive plasma). Integration of the ambipolar electric field results in a positive electrostatic plasma potential,  $\phi_p$ , which serves to trap or slow electrons from leaving the plasma and accelerate ions out of the plasma. This electric field is measured using the plasma potential measured by the emissive probe as described above.

The computed ambipolar electrostatic field (as vectors) and plasma potential (as color contours) are shown in Fig. 12 for an Ar pressure of 10 mTorr and a generator power of 300 W. The electric field is shown on two orthogonal planes, one perpendicular to the wafer and the other parallel to the wafer at a height of 8 cm. The 2 MHz coil frequency was observed on the plasma potential as a 10% ripple, which is produced in part by capacitive coupling and in part by oscillation in the electron temperature during the RF cycle. The maximum plasma potential at the center of the plasma is 17 V. The results from the model predict a maximum plasma potential of 23 V [Fig. 6(c)], which aligns with the 0.5 eV higher electron temperature predicted by the model compared to experiment.

The electromagnetic component of the internal electric field is a superposition of the electric field due to the changing RF coil currents, plasma currents, and image currents in the walls. The measured plasma current (Fig. 9) is in the same direction as the azimuthal electric field. There are no appreciable radial or vertical currents. This implies that the RF electric field,  $\vec{E}_{ind}$ , is primarily in the azimuthal direction. Since the wall currents can only be estimated, it is difficult to calculate the inductive component of the electric field from  $-\frac{\partial\vec{A}}{\partial t}$ . Instead, we apply Faraday's law,  $\int \vec{E}_{ind} \cdot d\vec{l} = -\frac{\partial}{\partial t} \int \vec{B} \cdot \hat{n} d\vec{A}$ , to the azimuthal component  $E_\phi$  from the time derivative of  $B_z$ . From the measured time derivative of  $\dot{B}_z$ , we get

$$E_\phi(r) = \frac{1}{2\pi r} \int_0^r \dot{B}_z(r') 2\pi r' dr' \tag{7}$$

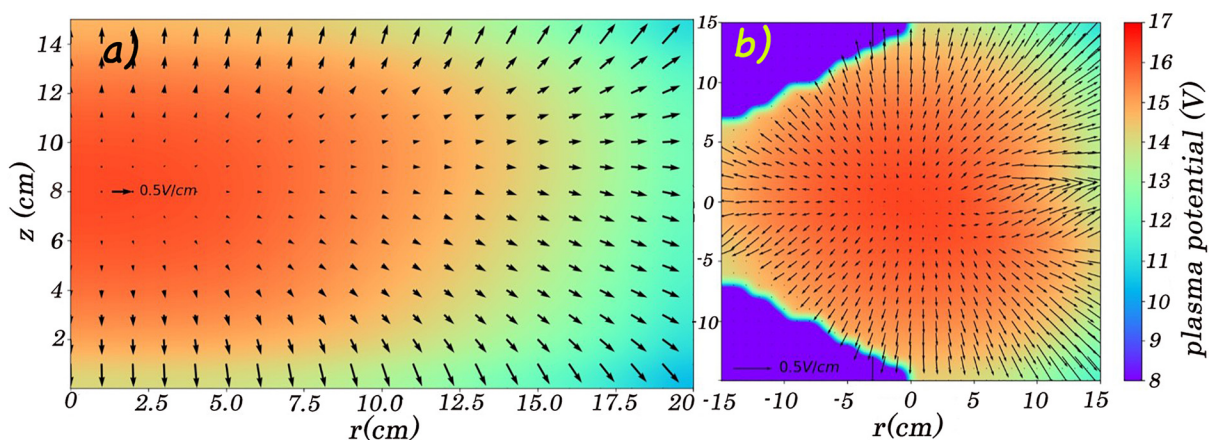


FIG. 12. Space charge electric field vectors calculated from measurements of the plasma potential (shown as flood contours) obtained by using an emissive probe for an Ar pressure of 10 mTorr and a generator power of 300 W. (a)  $E_x$ - $E_z$  vectors on a plane centered at  $y = 0$  where  $r = 0$  corresponds to the center of the wafer. (b).  $E_x$ - $E_y$  vectors on a plane-parallel to the wafer at an intermediate height,  $z = 8$  cm.

The RF electric field,  $E_{ind}$ , is shown in Fig. 13 for a 300 W 10 mTorr plasma at a vertical location just under the ceramic window,  $z = 13$  cm, and near the midplane of the chamber,  $z = 8$  cm. For comparison, the vacuum  $E_{ind}$  is shown for the same antenna current.  $E_{ind}$  results from oscillation in the vector potential that originates from the RF magnetic fields produced by the antenna. The induced electric field in the bulk of the plasma is diminished from the vacuum case because of the shielding effect of induced currents under the antenna. The magnitude of  $E_{ind}$  is comparable in the plasma and in vacuum near the top of the reactor where the electromagnetic wave from the coil has not been significantly absorbed. As one moves toward the wafer, the magnitude of  $E_{ind}$  decreases over a distance which exceeds the collisionless skin depth,  $\delta = c/\omega_p$ , where  $\omega_p$  is the electron plasma frequency.  $\delta$  is

7 mm in the center of the device and 1.6 cm near the coil. For a fully collisional plasma,  $\delta = \sqrt{2/\omega\mu_0\sigma} \approx 3.6$  cm near the coil. (Values for the collisional skin depth are discussed below.) There is generally a phase difference between the induced electric field in vacuum with respect to the plasma.

The RF electric field,  $E_{ind}$ , displayed as arrows on two planes ( $z = 8$  cm and  $z = 13$  cm) above the wafer is shown in Fig. 14. The power density  $P = 0.1$  W/cm<sup>3</sup> is depicted as a colored isosurface. Closer to the coil, the power is higher than 0.1 W/cm<sup>3</sup>.

#### D. Power deposition

The bulk of the power absorption is localized almost directly under the coil as this is where the image current from the coil is the largest.

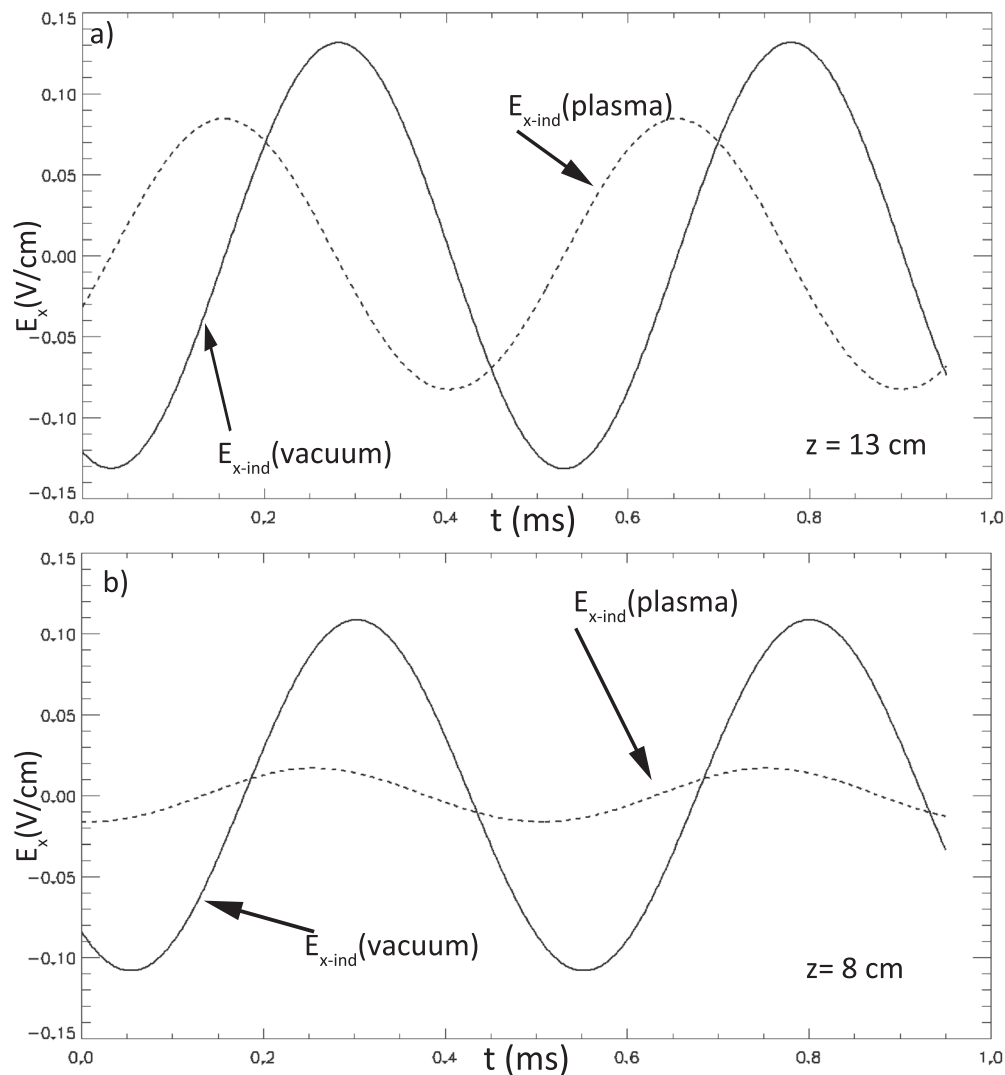


**FIG. 13.** The azimuthal component of the induced electric field,  $E_{ind}$ , during 2 RF cycles in vacuum (solid line) and in the plasma (dashed line). The Ar pressure is 10 mTorr, the total power is 300 W, and the coils are located at  $z = -20.6$  cm. (a)  $z = 13$  cm and (b)  $z = 8$  cm above the wafer. The  $(x,y)$  locations are (5.0 cm, 11.0 cm). The data were acquired 2.75 ms after the plasma was switched on.

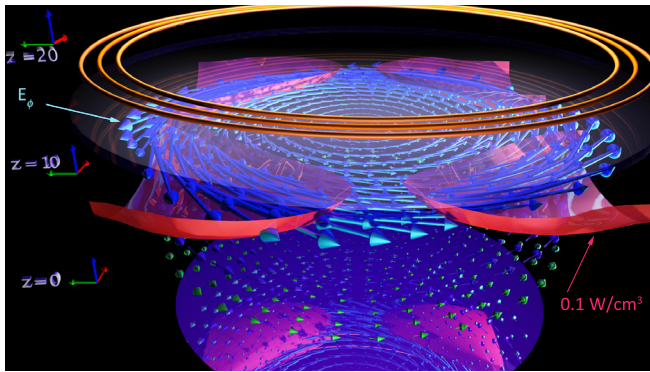


**FIG. 14.** Measured electromagnetic electric field shown as arrows in two planes above the wafer ( $z = 6$  and  $14$  cm) and an isosurface of power  $0.1 \text{ W/cm}^3$  shown in red at its maximum value during the RF cycle. The Ar pressure is 10 mTorr, and the generator power is 300 W. The RF coils and wafer ( $z = 0$ ) are shown to guide the eye. The axes arrow markers are green-y direction, red-x direction, and blue-z direction.

The time averaged power density inside the plasma calculated using  $P = \vec{j} \cdot \vec{E}$  is shown in Fig. 15(a) for a pressure of 10 mTorr and a generator power of 300 W. The feedstock gas flow rate affects the plasma current and electric field. At an increased flow rate, while keeping the chamber pressure and input power constant, we observed that plasma currents tended to be higher and more localized near the coil. Increasing the flow rate by a factor of two at constant power and pressure resulted in approximately a 30% increase in peak plasma current and at the same time 30% decrease in internal electric fields. The flow rate does not linearly impact plasma quantities, and further investigations are necessary to determine the effects of flow on other plasma properties (e.g., on metastable densities). The power deposition profiles at a high flow rate mimicked the higher pressure cases shown in Fig. 15, which similarly tend to localize the power deposition closer to the coil.

The inertial transport that leads to out-of-phase current density also produces instantaneous regions of positive and negative power deposition—regions where net power flows from the field into the plasma and regions where net power flow from the plasma back into the field. Although in most cases, the local, time averaged power deposition is positive, under select conditions, the cycle averaged power deposition can be locally negative. This has been observed by Godyak *et al.*<sup>25</sup> at 13.56 MHz and 6.78 MHz but not at 3.39 MHz. For our 300 W 10 mT argon discharge operating at 2 MHz, computed instantaneous power deposition is shown in Fig. 16 for the phase during which the striations between positive and negative power deposition are more pronounced. The results are shown for different modes of power deposition and pressures. Local refers to power in the calculation being given by  $\sigma E^2$ . Nonlocal refers to power in the calculation being given by where the current density is kinetically derived from electron trajectories produced in the *eMCS*. Similar experimental results for instantaneous power deposition are shown in Fig. 17 for pressures of 10, 50, and 100 mTorr. These results were obtained from instantaneous measured values of  $J$  and  $E$  and show regions of positive and negative power deposition.

At low pressure with nonlocal power deposition, the out-of-phase electrons produce a wavelike propagation of negative power deposition into the plasma, as shown in Fig. 16(a), similar to the current density

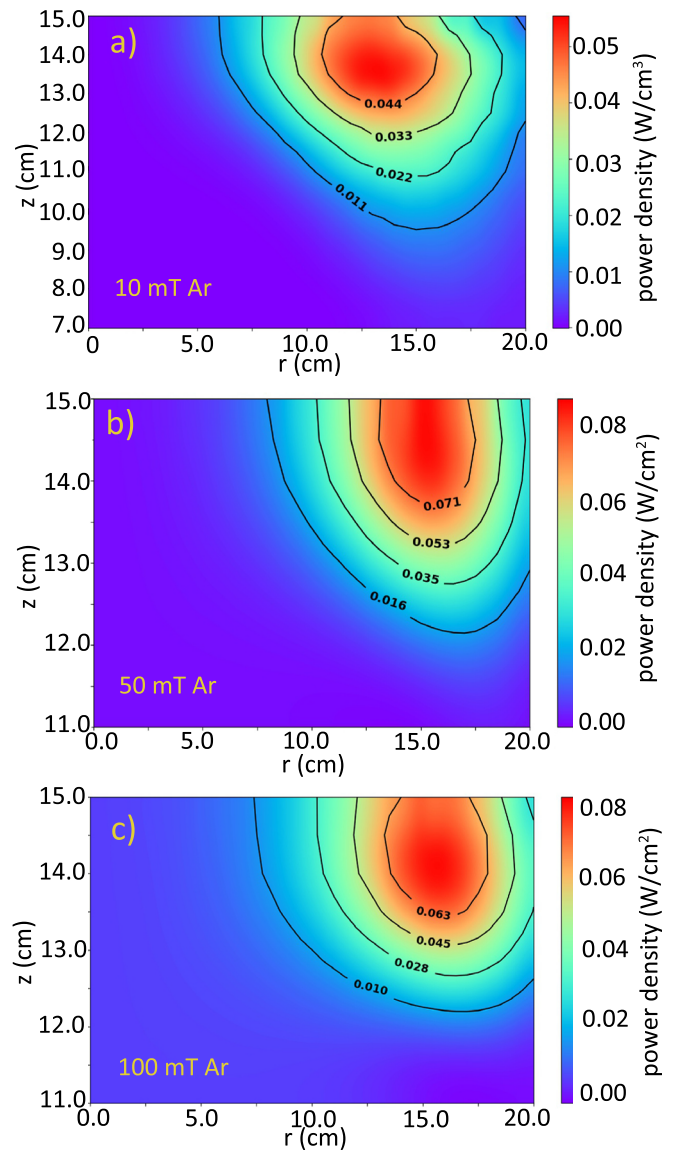


**FIG. 15.** Time averaged power density ( $\text{W/cm}^3$ ) calculated from  $P = \vec{j} \cdot \vec{E}$  for Argon pressures of (a) 10 mTorr, (b) 50 mTorr, and (c) 100 mTorr. The powers are plotted as a function of height and radius with the center of the wafer at  $r = 0$ . The mean coil radius is 18 cm, and the bulk of the power absorption occurs a few centimeters inward in radius and just under the top ceramic. Note that the vertical axis in Fig. 15(a) has a larger range than in Figs. 15(b) and 15(c).

shown in Fig. 10. With  $\omega/\nu_m = 0.45\text{--}0.5$ , as derived by the model, the plasma is reasonably collisional while still having reactive properties. The degree to which nonlocal transport affects the negative power deposition is shown in Fig. 16(b), also 10 mTorr, but where current density is given by  $\sigma E$ . With  $\sigma$  given by Eq. 5(b), the inertial (reactive) component of the conductivity is retained, whereas the nonlocal character is not. The general characteristics of the negative power are retained, whereas the phase at which the negative power is maximum decreases. (This decrease in phase is responsible for the decrease

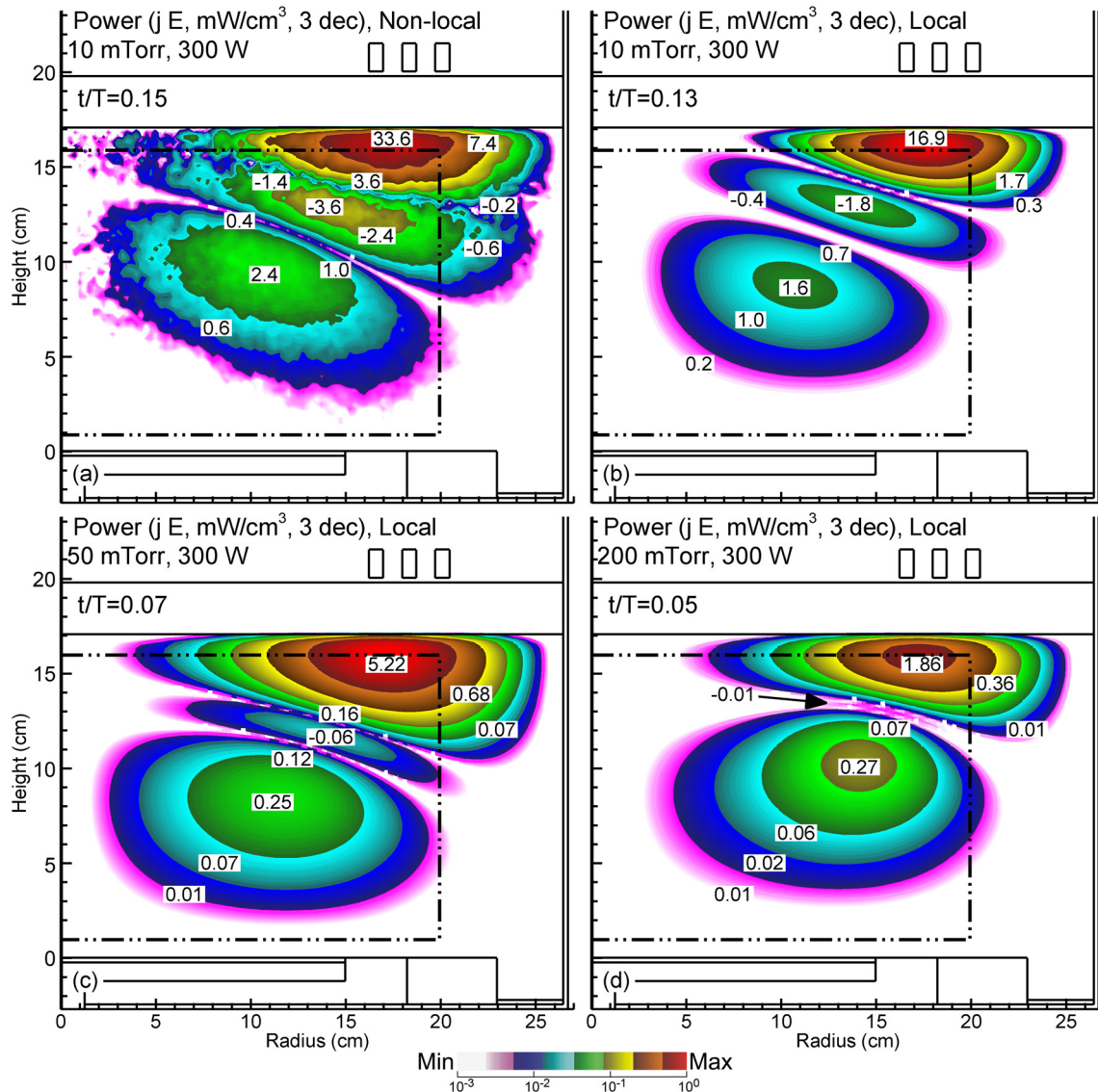


**FIG. 16.** Computed instantaneous power deposition for argon with 300 W of in-plasma power with the time in each cycle indicated. Color contours are power deposition plotted over 3 decades. Contour labels are in units of  $\text{mW}/\text{cm}^3$ . (a) 10 mTorr with nonlocal power deposition computed with the eMCS. (b) 10 mTorr, (c) 50 mTorr, and (d) 200 mTorr with local power deposition. The dotted-dashed line is the experimental view.

in magnitudes of both positive and negative powers.) With local transport, both the positive and negative power deposition extend over more limited space. With an increase in pressure to 50 mTorr [Fig. 16(c)] with local power deposition and  $\omega/\nu_m = 0.07\text{--}0.08$ , the region of negative power deposition shrinks and the phase at maximum negative power decreases, commensurate with the dephasing time of the electrons also decreasing. Finally, at 200 mTorr [Fig. 16(d)] with  $\omega/\nu_m = 0.02$ , the negative power deposition is nominal, as electrons dephase earlier in the RF cycle compared to the lower pressures having lower collision frequencies.

We note that the negative power dissipation in this experiment is small, much less than one percent of the total. Negative power

dissipation is only clearly displayed when experimental data or simulation results are plotted on a log scale as shown in Figs. 16 and 17.

RF power from the generator was calculated by measuring current and voltage at its terminals. These values are substantially in phase, although an exact multiplication over many cycles was performed prior to computing the average value. Power lost in the antenna and the RF delivery system between the generator and plasma is a few percent. To validate these measurements, we placed a 1-turn loop just above the RF antenna, with a resistor in series, while making no other changes to the system. Dissipation in the inductively coupled test circuit is measured by computing  $I^2R$  in the absence of plasma, at the same antenna current, with the same “match” settings. The power dissipated in the

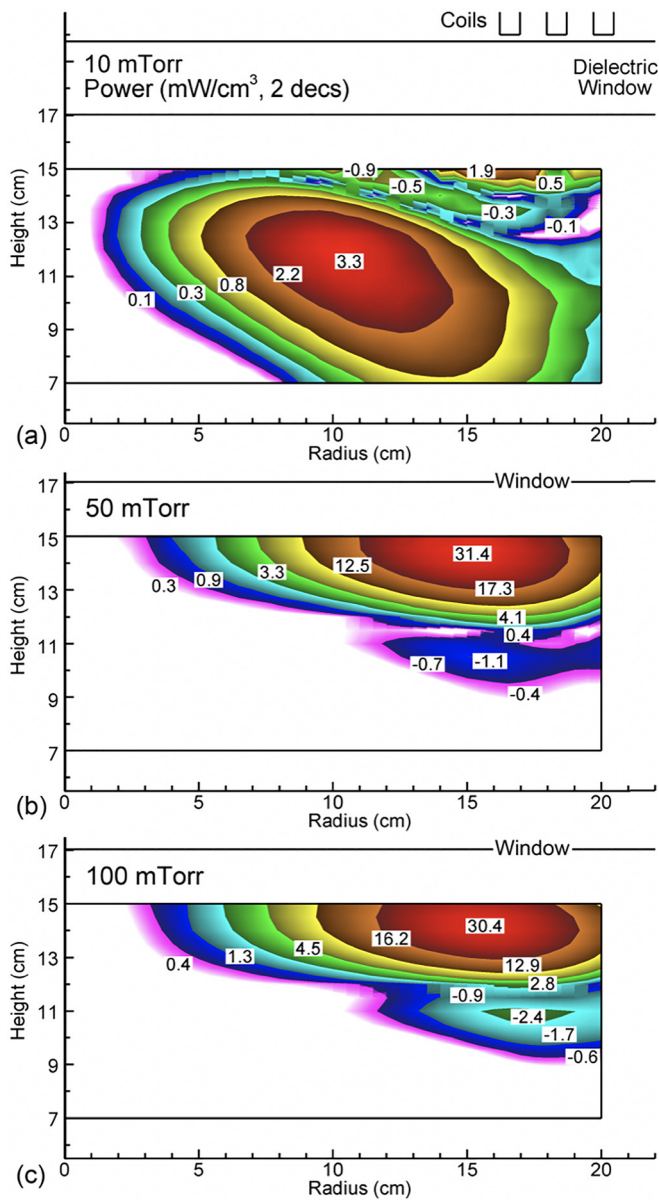


**FIG. 17.** Experimentally measured instantaneous power deposition ( $\text{mW}/\text{cm}^3$ ) for argon at pressures of (a) 10 mTorr, (b) 50 mTorr, and (c) 100 mTorr at 300 W. The phase of each image was chosen to emphasize the negative power deposition.

dummy load arrangement was within a few percent of the reported generator power at all relevant powers. These cross-checks provide confidence in the accuracy of the power being delivered to the plasma.

Once the power density is computed throughout space, we integrate over the volume to compute the measured total power dissipated in the plasma. Resistive losses in the system were estimated by measuring the generator power required to drive the corresponding equivalent coil currents with the chamber evacuated (that is, no plasma). The resistive losses are manifested primarily in coil heating and account for 10%–13% of the generator power. Since the viewpoint of

the experiment does not cover the entire volume of the plasma, the model was used to rescale the experimentally derived power deposition to that deposited in the entire reactor.

For example, at 10 mTorr, using nonlocal electron transport, results from the model indicate that the fraction of power deposition observable in the view of the experiment is about  $0.7 \pm 0.1$  of the total (based on the window and positioning uncertainty). The observable experimental power deposition for 10 mTorr and 300 W delivered from the generator is about 112.8 W. With recalibration from the model, the total power deposition in the plasma is then  $158.9 \pm 17$  W. Adding in the resistive power loss of  $42.1 \pm 2$  W produces a total of  $201 \pm 17$  W (see Table I). There is an unaccounted for power deposition of 99 W or about 33%. We expect that some fraction of the missing power is absorbed by the plasma through capacitive coupling. We measured oscillations in plasma potential using an emissive probe with a bandwidth of 20 MHz and calculated the RF variation in  $\vec{E}(\vec{r})$  from  $\vec{E} = -\nabla\phi_p$ . The estimated power density from capacitive coupling in the volume of the plasma,  $P = \sigma E^2$ , is few percent of the total or about 10 W. Measurements could not be performed in the sheath directly under the coil, which might account for additional power dissipation by ion acceleration by capacitive electric fields from the coil. However, based on results from the model, we estimate the loss due to ion acceleration under the coil to be about 20 W, which produces a total of about  $231 \pm 17$  W. For the rest of the entries in the table, we estimated capacitive losses as 10% of the generator power. With the uncertainty in the measurements of about 5%–10%, the majority of power deposition can be accounted for.

### E. Poynting Flux and Power Dissipation

Using the complete data for magnetic and electric fields, the Poynting flux,  $\vec{S} = \frac{1}{\mu_0} \vec{E} \times \vec{B}$ , can be computed. A composite of the experimentally measured plasma density, current density, Poynting flux, and absorbed power during steady state operation is shown in Fig. 18 for an Ar pressure of 10 mTorr and a generator power of 300 W. Except for the current density which is shown as a peak value, these quantities are averaged over the RF cycle. The plasma density is the largest in the center of the chamber and is not coincident with the plasma current density (grey contours above the red density contours). The Poynting flux originates at the coils and points toward the power deposition region. The maximum absorption is not coincident with the center of the current channel. The Poynting flux averaged over radius as a function of height for the same temporal interval as shown in Fig. 13 is shown in Fig. 19. The net Poynting flux briefly points upwards, toward the coil, twice each cycle. During a complete cycle, the integrated upward Poynting flux is 0.2 of the downward Poynting flux. The cycle averaged Poynting flux is downwards through the lid and estimated to be  $90 \text{ mW}/\text{cm}^2$ , for a total power of 110 W into the surface of the measurement volume. This compares favorably with the computed power in this volume of 113 W. In a purely nondissipative, reactive plasma where  $\omega/\nu_m \gg 1$ , the downward and upward directed Poynting fluxes would be symmetric over the RF cycle. There would be no net power deposition in the plasma as electrons remove power from the field on the first half cycle and give back power to the field on the latter half cycle. The differences between the downward and upward directed Poynting fluxes are a measure of the collisional power deposition.

**TABLE I.** Power deposition computed as the volume integral of  $\vec{J} \cdot \vec{E}$  with recalibration by the model to account for unobserved volumes of the reactor and coil resistive losses as a function of generator power for Ar plasmas at 10 mTorr. The renormalized power is the experimental power divided by fraction of power inside the view window.

Generator power (W)	Antenna resistive loss (W)	Experimental J.E (W)	Fraction of power inside view-window	Renormalized power (W)	10% Capacitive (W)	Total renormalized (W)	Power accounted for (%)
80	35.1	24.6	0.782	31.4	8	74.5	93.1
300	42.1	112.8	0.71	158.9	30	231.0	77.0
500	70.2	194.7	0.657	296.4	50	416.6	83.3
800	96.5	291.2	0.619	470.5	80	647.0	80.9

Properties of the Poynting vector obtained with the model are shown in Fig. 20 for a 300 W plasma sustained at 10 mTorr. The power transport model is nonlocal using the eMCS. The contours show the magnitude of the Poynting vector plotted on a log scale from 0.01–2.5 W/cm<sup>2</sup>. The arrows show only the direction (and not magnitude). The results are shown for 4 phases during the RF cycle chosen to demonstrate the change in the direction of the Poynting vectors. The first frame (t/T = 0.41) is when the Poynting vector is maximum pointing downward at 2.5 W/cm<sup>2</sup>, delivering power to the plasma. All Poynting vectors with magnitude larger than 10 mW/cm<sup>2</sup> point downwards. At t/T = 0.58, the direction of the Poynting vector near the coils has reversed to point upwards, taking power out of the plasma with a maximum amplitude of 0.9 W/cm<sup>2</sup>. At this time, power lower in the reactor continues to flow downward. At t/T = 0.64, the upward directed Poynting vector has its maximum value at 1.4 W/cm<sup>2</sup>. Essentially, all Poynting vectors greater than 10 mW/cm<sup>2</sup> are pointed upwards. Finally, at t/T = 0.78, power is again delivered from the antenna to the plasma with downward Poynting vector with a magnitude of 0.8 W/cm<sup>2</sup>, while in the fringes of the skin depth, power is still directed upwards.

**F. Plasma conductivity**

The electron drift velocity is given by

$$\frac{\partial \vec{v}_d(\vec{r}, t)}{\partial t} = \frac{q\vec{E}(\vec{r}, t)}{m_e} - \nu_m \vec{v}_d(\vec{r}, t). \tag{8}$$

With  $\vec{v}_d$  and  $\vec{E}$ , both having a harmonic time dependence  $\exp(i\omega t)$ , the solution is

$$\vec{v}_d(\vec{r}) = \frac{q\vec{E}(\vec{r})}{m_e \nu_m(\vec{r}) \left(1 + i \frac{\omega}{\nu_m(\vec{r})}\right)}, \tag{9}$$

and the plasma current density is then  $\vec{J}(\vec{r}) = qn_e(\vec{r})\vec{v}_d(\vec{r})$ , which results in the plasma conductivity given in Eq. (5). There is a phase difference between  $\vec{J}(\vec{r})$  and  $\vec{E}(\vec{r})$  due to electron inertia, represented by the imaginary component in the denominator of the conductivity.<sup>26,27</sup> By comparing the measured values of  $\vec{J}(\vec{r})$  and  $\vec{E}(\vec{r})$ , we compute experimental values for the magnitude and phase of the conductivity  $\sigma = |\frac{J}{E}|e^{i\gamma}$ . Experimentally, we find the phase difference ( $\gamma$ ) varies between 10° and 20° at most locations in the plasma, corresponding

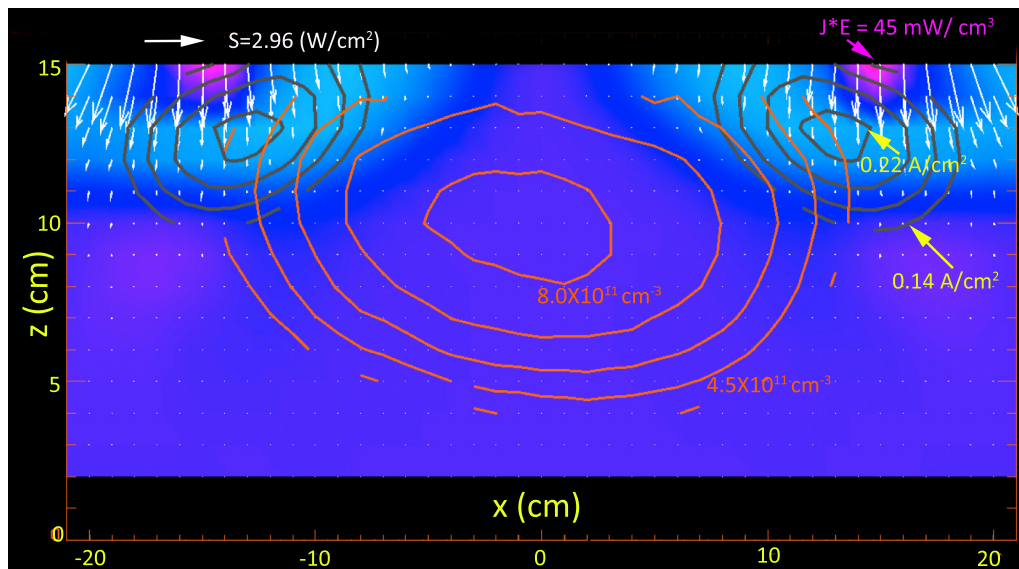


**FIG. 18.** Contours of plasma density (red), shaded contours of plasma dissipation. The Poynting flux is shown as white arrows and the plasma current density as brown contours. Values are shown for an Ar pressure of 10 mTorr and a generator power of 300 W.

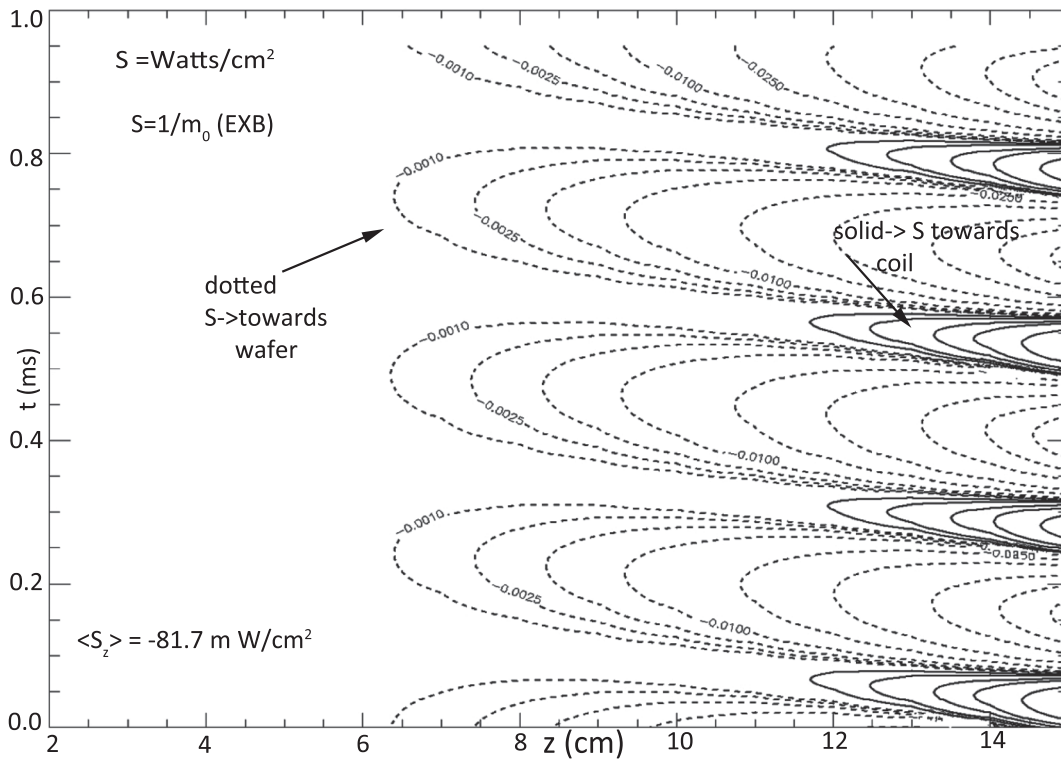


**FIG. 19.** Poynting flux averaged over radius and as a function of height above the wafer. The solid curves depict power directed upwards toward the coil. The dashed lines indicate power flow toward the wafer. In the presence of plasma, they are not symmetric. The downward Poynting flux averaged over the two cycles shown is  $-81.7 \text{ mW/cm}^2$ . The largest downward flux is  $-496 \text{ mW/cm}^2$ , and the largest upward Poynting flux is  $201.0 \text{ mW/cm}^2$ .

to  $\nu_m \geq 3\omega$ . The phase difference  $\gamma$  is the largest near the top of the chamber in agreement with the simulation, potentially due to nonlocal effects arising in the strong electric field region under the coil. The real part of the conductivity  $\text{Re}[\sigma] = |\sigma| \cos(\gamma)$  obtained from experiment and simulation is shown in Fig. 21. Since both the electric field and current density are small near the bottom and center of the experimental chamber, their ratio develops large errors due to measurement noise, and so the conductivity is evaluated only for  $r > 3.5 \text{ cm}$ ,  $z > 8 \text{ cm}$ . The simulations computed the conductivity in the same manner as derived in experiments. The complex electric field was obtained from the solution of Maxwell's equation. The complex current density was obtained from Fourier analysis of trajectories of pseudoparticles in the electron Monte Carlo simulation. Complex conductivity was then computed as  $\sigma = \frac{J}{E} |e^{i\gamma}$ . The spatial profiles for real conductivity agree within a factor of two, with the differences in the large part due to the difference in  $\omega/\nu_m$ . With this conductivity profile, the collisional skin depth ranges from ten centimeters in the low plasma density region under the coil to a few centimeters where the conductivity is the largest in the center of the plasma. If plasma conductivity strictly obeys Eq. (5), one expects its spatial dependence to match the electron density, when  $T_e$  is spatially uniform, which is generally the case.

The measured conductivity cannot be explained with a simple Ohms law as the electron dynamics are nonlocal. Fast electrons are generated in the narrow sheath under the RF coil and stream

downward into the region where the power dissipation is the largest. The electron distribution function is an amalgam of bulk and tail electrons, each coming from different locations. This is what makes the phenomena nonlocal—an electric field applied to one part of the plasma has an influence on the current density elsewhere due to long mean-free-path transport.<sup>28</sup> Changes in conductivity due to the anomalous skin effect have been reported by Kolobov and Economou,<sup>29</sup> Lafleur *et al.*,<sup>30</sup> and Cunge *et al.*,<sup>28</sup> with theory initially developed by Weibel.<sup>31</sup> This anomalous transport contributes to the phase difference between electric field and current density that conventional theory attributes solely to local inertial effects of the electrons oscillating in a harmonic field.

#### IV. DISCUSSION AND CONCLUSIONS

Understanding the physics of low temperature plasmas and translation of those findings to industrial use requires measurements of fundamental quantities such as magnetic field, total electric field, plasma density and temperature, optimally performed in three dimensions. In this investigation, 3D measurements of these quantities were obtained for the quasi-steady state of a pulsed ICP sustained in argon in an industrial plasma reactor modified to enable probe access. With these measurements, internal plasma current, power dissipation, and Poynting flux were derived. We found that the peaks of plasma density, current, power deposition, and Poynting flux were not spatially coincident. Although this is an expected result at lower pressures and

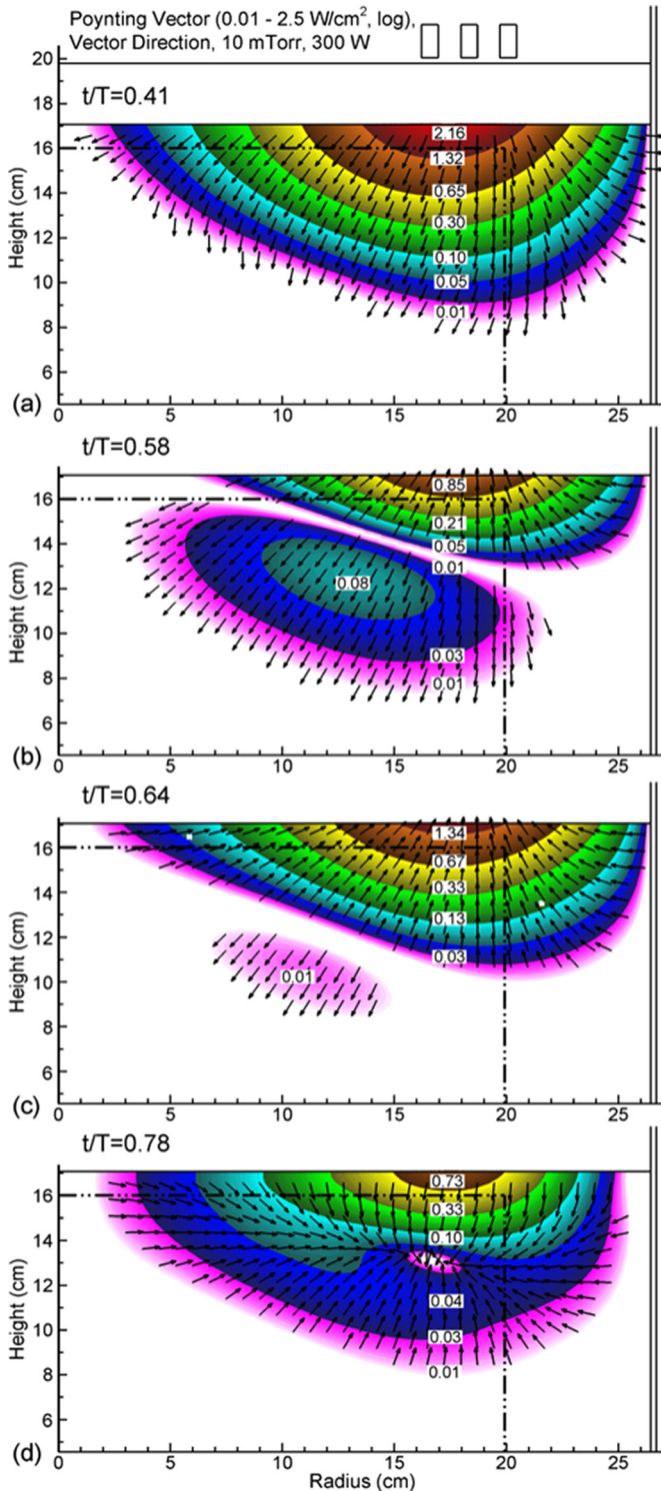


**FIG. 20.** Magnitude of Poynting vector ( $W/cm^2$ ) and direction of vector for different times during the RF cycle. (a)  $t/T = 0.41$ , (b)  $0.58$ , (c)  $0.64$ , and (d)  $0.78$ . Plasma conditions are Ar, 10 mTorr, 300 W. The contours are plotted on a log scale ( $0.01$ – $2.5 W/cm^2$ ). The arrows have constant length to show direction only.

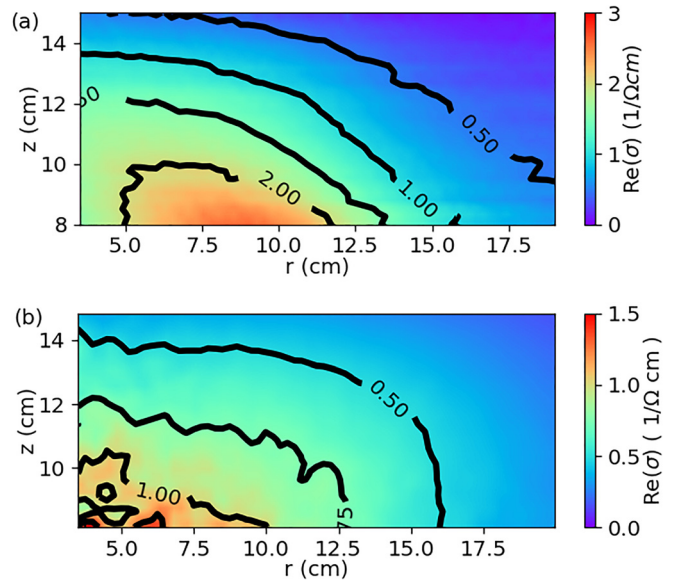


**FIG. 21.** Real component of the conductivity throughout the plasma ( $1/\Omega\text{-cm}$ ) obtained from (a) experimental values of  $J$  and  $E$  and (b) simulation results computed in the same fashion.

higher powers where diffusion dominates and electron thermal conductivity is high, at the moderate pressures and power of this investigation, we might expect that plasma density would be more localized closer to the region of power deposition. The measurements imply that either convective noncollisional transport of electrons in the tail of the distribution or rapid thermal conduction, both of which would more uniformly distribute ionization throughout the reactor, retains their influence at these higher pressures and lower power deposition.

From the plasma temperature measurement, we derived the electrostatic part of  $\vec{E}$  which points away from the center where the electron density is a maximum. From the momentum transfer equation, the divergence of the pressure tensor gives the change of momentum flux due to spatial inhomogeneities. Since the electron temperature is nearly spatially uniform, this inhomogeneity arises from gradients in charge density. The uniformity of  $T_e$  indicates a high electron thermal conductivity, since measured power deposition is highly nonuniform.

The volumetric magnetic field measured by three loops oriented in perpendicular directions was used to derive the current density and electromagnetic part of  $\vec{E}(r, z)$ . These 3D measurements demonstrate and confirm azimuthal symmetry in a cylindrical stove top ICP, symmetries that previously were assumed to apply. Plasma current peaks slightly inwards underneath the antenna, and the peak current density propagates downward. The fact that the current does not penetrate vertically downward in a straight line is due to a nonuniform conductivity. The computed power  $P = \vec{J} \cdot \vec{E}$  from probe measurements accounts for 80% of the generator power. Negative power deposition inside the volume indicates an inertial component of the electron current, and this is further supported by conductivity calculations.

These measurements, and accompanying modeling, have contributed to quantifying physical phenomena necessary to understand fundamental plasma transport in ICP chambers. The measurements here may also contribute to understanding the electron kinetics of

other applications such as electric propulsion and the temporal behavior of the electromagnetics in magnetic nozzles.<sup>32</sup> The simultaneous, multi-dimensional, and time-dependent measurements of nearly all pertinent plasma properties have enabled confirmation and clarification of the global mode of operation of ICPs of industrial interest.

### SUPPLEMENTARY MATERIAL

See the [supplementary material](#) for animations of the 3D measurements.

### ACKNOWLEDGMENTS

This work was supported by the National Science Foundation (Nos. PHY-1500099 and PHY1500126), the Department of Energy Office of Fusion Energy Science (Nos. DE-SC0001319 and DE-SC0014132), and Lam Research Corp. We thank Lam Research Corp. for the donation of the plasma chamber. We acknowledge the expert technical help of Zalton Lucky, Tai Ly, and Marvin Drandell.

### REFERENCES

- <sup>1</sup>M. A. Lieberman and A. J. Lichtenberg, *Principles of Plasma Discharges and Materials Processing* (Wiley Interscience, 1994), p 388.
- <sup>2</sup>R. Piejak, V. Godyak, and B. Alexandrovich, "Magnetic field distribution measurements in a low-pressure inductive discharge," *J. Appl. Phys.* **78**, 9 (1995).
- <sup>3</sup>R. Piejak, V. Godyak, and B. Alexandrovich, "The electric field and current density in a low-pressure inductive discharge measured with different B-dot probes," *J. Appl. Phys.* **81**(8), 3416 (1997).
- <sup>4</sup>J. Hopwood, C. R. Guarnieri, S. J. Whitehair, and J. J. Cuomo, "Electromagnetic fields in a radio-frequency induction plasma," *J. Vac. Sci. Technol., A* **11**, 147 (1993).
- <sup>5</sup>R. Limpaecher and K. R. McKenzie, "Magnetic multipole containment of large collisionless quiescent plasmas," *Rev. Sci. Instrum.* **44**, 726 (1973).
- <sup>6</sup>M. El-Fayoumi and I. R. Jones, "Theoretical and experimental investigations of the electromagnetic field within a planar coil, inductively coupled RF plasma source," *Plasma Sources Sci. Technol.* **7**, 162 (1998).
- <sup>7</sup>M. Tuszewski, "Particle and heat transport in a low-frequency inductively coupled plasma," *Phys. Plasma* **5**, 1198 (1998).
- <sup>8</sup>S. Srinivasan, J. Marquis, L. Pratti, M. H. Khater, M. J. Goekner, and L. J. Overzet, "The effects on plasma properties of a current node on inductively coupled plasma sources," *Plasma Sources Sci. Technol.* **12**, 432 (2003).
- <sup>9</sup>Z. F. Ding, B. Sun, and W. G. Huo, "Characteristics of anomalous skin effect and evolution of power absorption regions in a cylindrical radio frequency inductively coupled plasma," *Phys. Plasmas* **22**, 063504 (2015).
- <sup>10</sup>V. A. Godyak and R. B. Piejak, "Electromagnetic field structure in a weakly collisional inductively coupled plasma," *J. Appl. Phys.* **82**, 5944 (1997).
- <sup>11</sup>V. Godyak, R. Piejak, and B. Alexandrovich, "Observation of second harmonic currents in inductively coupled plasmas," *Phys. Rev. Lett.* **83**, 1610 (1999).
- <sup>12</sup>K. Ostrikov, E. Tsakadze, S. Xu, S. V. Vladimirov, and R. Storer, "Nonlinear electromagnetic fields in 0.5 MHz inductively coupled plasmas," *Phys Plasmas* **10**, 1146 (2003).
- <sup>13</sup>P. Subramonium and M. J. Kushner, "Pulsed plasmas as a method to improve uniformity during materials processing," *J. Appl. Phys.* **96**, 82 (2004).
- <sup>14</sup>D. Leneman and W. Gekelman, "A Novel angular motion feedthrough," *Rev. Sci. Instrum.* **72**, 3473 (2001).
- <sup>15</sup>J. P. Sheehan and N. Hershkowitz, "Emissive probes," *Plasma Sources Sci. Technol.* **20**, 063001 (2011).
- <sup>16</sup>M. J. Martin, J. Bonde, W. Gekelman, and P. Pribyl, "A resistively heated CeB6 emissive probe," *Rev. Sci. Instrum.* **86**, 053507 (2015).
- <sup>17</sup>J. Y. Kim *et al.*, "Investigation of the Boltzmann relation in plasmas with non-Maxwellian electron distribution," *Phys. Plasmas* **21**, 023511 (2014).
- <sup>18</sup>T. Hori, M. D. Bowden, K. Uchino, and K. Muraoka, "Measurements of electron temperature, electron density, and neutral density in a radio-frequency inductively coupled plasma," *J. Vac. Sci. Technol., A* **14**, 144 (1996).
- <sup>19</sup>R. L. Stenzel, *Rev. Sci. Instrum.* **47**, 603 (1976).
- <sup>20</sup>X. Fan, P. Pribyl, J. Han, Y. Wug, and T. Carter, "Electron density measurement with hairpin resonator using modular electronics," *Rev. Sci. Instrum.* (unpublished).
- <sup>21</sup>R. L. Stenzel, "Whistler wave propagation in a large magnetoplasma," *Phys. Fluids* **19**, 857 (1976).
- <sup>22</sup>M. J. Kushner, "Hybrid modelling of low temperature plasmas for fundamental investigations and equipment design," *J. Phys. D* **42**, 194013 (2009).
- <sup>23</sup>P. Tian and M. J. Kushner, "Controlling VUV photon fluxes in low-pressure inductively coupled plasmas," *Plasma Sources Sci. Technol.* **24**, 034017 (2015).
- <sup>24</sup>A. V. Vasenkov and M. J. Kushner, "Electron energy distributions and anomalous skin depth effects in high-Plasma-density inductively coupled discharges," *Phys. Rev. E* **66**, 066411 (2002).
- <sup>25</sup>V. A. Godyak and V. I. Kolobov, "Negative power absorption in inductively coupled plasma," *Phys. Rev. Lett.* **79**, 4589 (1997).
- <sup>26</sup>G. G. Lister, Y. M. Li, and V. A. Godyak, "Electrical conductivity in high-frequency plasmas," *J. Appl. Phys.* **79**, 8993 (1996).
- <sup>27</sup>V. A. Godyak, R. B. Piejak, B. M. Alexandrovich, and V. I. Kolobov, "Experimental evidence of collisionless power absorption in inductively coupled plasma," *Phys. Rev. Lett.* **80**, 3264 (1998).
- <sup>28</sup>G. Cunge, B. Crowley, D. Vender, and M. M. Turner, "Anomalous skin effect and collisionless power dissipation in inductively coupled discharges," *J. Appl. Phys.* **89**, 3580 (2001).
- <sup>29</sup>V. I. Kolobov and D. J. Economou, "The anomalous skin effect in gas discharge plasma," *Plasma Sources Sci. Technol.* **6**(1), R1 (1997).
- <sup>30</sup>T. Lafleur, P. Chabert, M. M. Turner, and J. P. Booth, "Anomalous collisionality in low-pressure plasmas," *Phys. Plasmas* **20**, 124503 (2013).
- <sup>31</sup>E. S. Weibel, "Anomalous skin effect in a plasma," *Phys. Fluids* **10**, 741 (1967).
- <sup>32</sup>J. Y. Kim *et al.*, "Time dependent kinetic analysis of trapped electrons in a magnetically expanding plasma," *Plasma Sources Sci. Technol.* **28**, 07LT01 (2019).